



저작자표시-비영리-변경금지 2.0 대한민국

이용자는 아래의 조건을 따르는 경우에 한하여 자유롭게

- 이 저작물을 복제, 배포, 전송, 전시, 공연 및 방송할 수 있습니다.

다음과 같은 조건을 따라야 합니다:



저작자표시. 귀하는 원저작자를 표시하여야 합니다.



비영리. 귀하는 이 저작물을 영리 목적으로 이용할 수 없습니다.



변경금지. 귀하는 이 저작물을 개작, 변형 또는 가공할 수 없습니다.

- 귀하는, 이 저작물의 재이용이나 배포의 경우, 이 저작물에 적용된 이용허락조건을 명확하게 나타내어야 합니다.
- 저작권자로부터 별도의 허가를 받으면 이러한 조건들은 적용되지 않습니다.

저작권법에 따른 이용자의 권리는 위의 내용에 의하여 영향을 받지 않습니다.

이것은 [이용허락규약\(Legal Code\)](#)을 이해하기 쉽게 요약한 것입니다.

[Disclaimer](#)

공학박사학위논문

**Multi-furcation assembly of charged aerosols  
and its application to gas sensing**

2017 년 2 월

서울대학교 대학원

기계항공공학부

배 용 준

## **Abstract**

# **Multi-furcation assembly of charged aerosols and its application to gas sensing**

Yongjun Bae  
School of Mechanical and Aerospace Engineering  
The Graduate School  
Seoul National University

In this thesis, we describe a simple yet practical parallel method to realize novel multi-furcated 3D micro/nanostructures by using the assembly of charged aerosols via spatial differentiation of electric field at atmospheric condition. A combination of generating charged aerosols by spark discharge and manipulating 3D electric field together with ion-induced electrostatic lenses lead to the formation of exotic 3D multi-furcated structures consisting of nanoparticles. By changing the arrangement of dielectric pre-patterns on the silicone substrate, bi-, tri-, tetra- or penta-furcated 3D nanoparticle structures and even interconnections between neighboring structures are precisely controlled. Based on these 3D multi-furcated micro/nanostructures, we propose a novel 3D gas sensor consisting of copper oxide nanoparticles, which exhibits excellent gas sensitivity significantly superior to that of two dimensional film type by more than 200 %. Also, we fabricate the sensor array with CuO and SnO<sub>2</sub> nanoparticle bridge structures to demonstrate the selective detecting of NO<sub>2</sub> and H<sub>2</sub>.

**Key Words :** Aerosol, Nanotechnology, Self-assembly, Nanoparticle assembly,  
Gas sensor

**Student Number:** 2010-20680

## Table of Contents

<b>Chapter 1. Introduction</b>	
1.1. Background of Research.....	2
1.2. Objectives for Research.....	5
1.3. References.....	6
<b>Chapter 2. Multi-furcation Growth of Charged Nano-aerosols via Ion Assisted Aerosol Lithography (IAAL)</b>	
2.1. Introduction.....	10
2.2. Method .....	13
2.2.1. Nanoparticle generations and characterizations	13
2.2.2. Spark discharge and Ion Assisted Aerosol Lithography (IAAL)	16
2.2.3. Numerical simulation for electric field calculation	23
2.2.4. Homemade Matlab code for the particle trajectory simulation	27
2.3. Results and Discussion .....	29
2.3.1. Formation of multi-directional assembly with charged nanoparticles	29
2.3.2. Particle assembly simulation for the bifurcation structure	35
2.3.3. Alignment distance and angle for the bifurcation growth	41
2.3.4. Multi-furcation and spontaneous connections between structures	44
2.4. Summary .....	51
2.5. References .....	52
<b>Chapter 3. Enhancement of the Metal Oxide Gas Sensor using Nano-aerosol Assembly Structures</b>	
3.1. Introduction.....	56
3.2. Method .....	58
3.2.1. Copper and tin nanoparticle generation and assembly	58
3.2.2. Characterization techniques	60
3.2.3. Gas sensor measurements	61
3.3. Results and Discussion .....	63
3.3.1. Network and interconnection with nanoparticle assembly	63
3.3.2. Sensitivity enhancement with multi-furcation structure of nanoparticle assembly	67
3.3.3. Selective detection of NO <sub>2</sub> and H <sub>2</sub> using heterogeneous metal oxide gas sensor array with nanoparticle assembly	77
3.4. Summary .....	90
3.5. References .....	91
국문초록 .....	93



# **Chapter 1.**

## **Introduction**

## **1.1. Background of Research**

The progress in nanotechnology has offered a range of nanostructures and textures for various applications. Due to their unique properties, studying nanostructures was prerequisite for both fundamental research and practical devices. In recent times, nano and microstructures have found widespread applications in various research fields. For example, they play an important role in many different experiments such as detecting molecules in the diluted mixture[1,2], enhancing performances of the optical devices with unique optical properties[3], mimicking interesting bio-systems[4,5], and demonstrating the electronic devices with nano-networks[6,7]. Especially nanostructures have been considered as a promising platform for various devices including sensors, solar cells, and fuel cells.

For the generation of the promising nanostructures, it is very important to understand the fabricating method and diverse forces applied on the nano and microscopic dimension. The nano-components including organic[8], inorganic[9], and biomolecule[10,11] have been applied to bottom up methods utilizing electric field[12,13], magnetic field[14], flow field[15], and even functional surface[16]. Even though the established assembly strategies can place the small elements at desired locations, it still remains challenging to fabricate the oriented structures with nano-compositions. In other words, a precise manner for nano-material

alignment is needed to control the position, growth orientation, and the growth rate of the structures.

For the nano-component patterning, dip-pen-lithography utilizing the capillary force between the AFM tip and substrate has been developed. As a serial method, dip-pen-lithography transfers various materials like nanoparticles, molecules, and proteins in the dot pattern or line pattern[17]. Recently, to fabricate arbitrary three dimensional (3D) shapes, hollow microfluidic AFM cantilevers, so-called FluidFM probes, were devised, which enabled the continuous deposition for the 3D structures by electroplating copper[18].

A nano-nozzle or pipette providing reliable nanomaterial supply has the ability to fabricate the fine structures. Nano-droplets and fibers of nanoparticles, carbon nano tubes, virus, and polymer materials could be generated with the nano-nozzle[19,20,21,22]. The generated nanomaterials from the nozzle are placed on the substrate with precisely controllable stages for the microscale fabrication of the complex 3D objects[23].

Also, the use of polymerizable resins was involved in the fabrication of 3D microstructures in various contexts. Instead of the single photon process showing the simple fabrication with the light intensity, the two photon direct laser writing has been proposed as a potential tool, which enables 3D spatial resolution. To prepare the 3D conductive structures, furthermore, photoreduction of metallic ions was used and developed[24]. In addition, for high resolution, resist-free, and

direct writing, focused electron beam induced deposition was designed. As dissociating and depositing adsorbed precursor molecules, focused electron beam was able to fabricate complicate structures like fullerene shaped structures [25].

In chemical based processes, depending on crystallinity of materials, various types of 3D structures are grown like nanowire, nano-flower, and so on[1,5,26,27]. Through the precise design, the connection between the nanowires could be fabricated[26]. Also, crossed nanowires were demonstrated with repositioning the catalyst at the end of the nanowires to alter the growth direction[27].

An ion induced focusing concept has been introduced to precipitate the charged aerosols and focus them via electrostatic lens on the substrate. Through this method, particles could be patterned with nanometer scale resolution and assembled for 3D nanoparticle structure arrays[13,28]. In this work, we develop a method for fabricating exotic 3D structures like multi-furcation growth structures. Also, the nanoparticle assembly method is combined with a gas sensor device for realizing an increase in sensitivity and selectivity of the sensor.

## **1.2. Objectives for Research**

In this research, we pursue developing a reliable assembly method of charged nano-aerosols for multi-furcation structures and applying the structures on a device. To realize the goal, we designed a multi-directional growth assembly of charged nanoparticles and spontaneous connections between structures. Next, we found a gas sensor as an application utilizing these structures.

First, we proposed a versatile method to control the growth direction of the nanoparticle assembly with a distorted electric field on the substrate, which guides the charged aerosols to the bottom of the electric potential valley. So far, without highly precise design or stage control, controlling the growth direction of micro structures and connecting between structures have been still challenging.

Second, we demonstrated the multi-furcated bridging gas sensor as one illustration of numerous possibilities of the 3D assembly method.

### 1.3. References

- [1] L. Soleymani, Z. Fang, E. H. Sargent, S. O. Kelley, *Nature Nanotechnol.* 2009, 4, 844.
- [2] A. Tricoli, S. E. Pratsinis, *Nature Nanotechnol.* 2009, 5, 54.
- [3] N. Liu, M. L. Tang, M. Hentschel, H. Giessen, A. P. Alivisatos, *Nature Mater.* 2011, 10, 631.
- [4] R. A. Potyrilo, H. Ghiradella, A. Vertiatchikh, K. Dovidenko, J. R. Cournoyer, E. Olson, *Nature Photon.* 2007, 1, 123.
- [5] W. L. Noorduin, A. Grinthal, L. Mahadevan, J. Aizenberg, *Science* 2013, 340, 832.
- [6] E. Miele, A. Accardo, A. Falqui, M. Marini, A. Giugni, M. Leoncini, F. D. Angelis, R. Krahne, E. D. Fabrizio, *Small* 2015, 11, 134.
- [7] S. Chen, M. Su, C. Zhang, M. Gao, B. Bao, Q. Yang, B. Su, Y. Song, *Adv. Mater.* 2015, 27, 3928.
- [8] P. Akcora, H. Liu, S. K. Kumar, J. Moll, Y. Li, B. C. Benicewicz, L. S. Schadler, D. Acehan, A. Z. Panagiotopoulos, V. Pryamitsyn, V. Ganesan, J. Ilavsky, P. Thiyagarajan, R. H. Colby, J. F. Douglas, *Nat. Mater.* 2009, 8, 354.
- [9] Z. Nie, A. Petukhova, E. Kumacheva, *Nat. Nanotech.* 2010, 5, 15.
- [10] S. Oh, E. Kwak, S. Jeon, S. Ahn, J. Kim, J. Jaworski, *Adv. Mater.* 2014, 26, 5217.
- [11] Y. Ke, L. L. Ong, W. M. Shih, P. Yin, *Science* 2012, 338, 1177.
- [12] A. Rotaru, J. Dugay, R. P. Tan, I. A. Guralskiy, L. Salmon, P. Demont, J. Carrey, G. Molnar, M. Respaud, A. Bousseksou, *Adv. Mater.* 2013, 25, 1745.
- [13] H. Kim, J. Kim, H. Yang, J. Suh, T. Kim, B. Han, S. Kim, D. S. Kim, P. V.

- Pikhitsa, M. Choi, *Nat. Nanotech.* 2006, 1, 117.
- [14] A. F. Demirors, P. P. Pillai, B. Kowalczyk, B. A. Grzybowski, *Nature* 2013, 503, 99.
- [15] T. Kraus, L. Malaquin, H. Schmid, W. Riess, N. D. Spencer, H. Wolf, *Nature Nanotech.* 2007, 2, 570.
- [16] A. H. Groschel, A. Walther, T. I. Lobling, F. H. Schacher, H. Schmalz, A. H. E. Muller, *Nature* 2013, 503, 247.
- [17] J. Zhao, L. A. Swartz, W. Lin, P. S. Schlenoff, J. Frommer, J. B. Schlenoff, G. Liu, *ACS Nano* 2016, 10, 5656.
- [18] D. Momotenko, A. Page, M. A. Vidal, P. R. Uniwin, *ACS Nano* 2016, 10, 8871.
- [19] P. Galliker, J. Schneider, H. Eghlidi, S. Kress, V. Sandoghdar, D. Poulidakos, *Nat. Commun.* 2012, 3, 890.
- [20] J. H. Kim, S. Lee, M. Wajahat, H. Jeong, W. S. Chang, H. J. Jeong, J. R. Yang, J. T. Kim, S. K. Seol, *ACS Nano* 2016, 10, 8879.
- [21] S. Oh, E. A. Kwak, S. Jeon, S. Ahn, J. M. Kim, J. Jaworski, *Adv. Mater* 2014, 26, 5217.
- [22] S. Y. Min, T. S. Kim, B. J. Kim, H. Cho, Y. Y. Noh, H. Yang, J. H. Cho, T. W. Lee, *Nat. Commun.* 2013, 4, 1773.
- [23] M. Panagiotakopoulou, M. Bergert, A. Taubenberger, J. Guck, D. Poulidakos, A. Ferrari, *ACS Nano* 2016, 10, 6437.
- [24] E. Blasco, J. Muller, P. Muller, V. Trouillet, M. Schon, T. Scherer, C. B. Kowollik, M. Wegener, *Adv. Mater.* 2016, 28, 3592.
- [25] J. D. Fowlkes, R. Winkler, B. B. Lewis, M. G. Stanford, H. Plank, P. D. Rack,

ACS Nano 2016, 10, 6163.

[26] D. Dalacu, A. Kam, D. G. Austing, P. J. Poole, Nano Lett. 2013, 13, 2676.

[27] S. R. Plissard, I. V. Weperen, D. Car, M. A. Verheijen, G. W. G. Immink, J. Kammhuber, L. J. Cornelissen, D. B. Szombati, A. Geresdi, S. M. Frolov, L. P. Kouwenhoven, E. P. A. M. Bakkers, Nat. Nanotechnol. 2013, 8, 859.

[28] H. Lee, S. You, P. V. Pikhitsa, J. Kim, S. Kwon, C. G. Woo, M. Choi, Nano Lett. 2011, 11, 119.

## **Chapter 2.**

# **Multi-furcation Growth of Charged Nano-aerosols via Ion Assisted Aerosol Lithography (IAAL)**

## 2.1. Introduction

Nano and microstructures have provided widespread applications in various research fields such as in sensing molecules in the diluted mixture,[1,2] developing the unique optical properties,[3] enhancing the nature inspired technology,[4,5] and fabricating the electronic devices with nano-networks.[6,7] Three dimensional (3D) micro/nanostructures could provide a new opportunity for various novel devices including sensors, solar and fuel cells,[8,9] and electronic devices. For this, the nano-components including organic,[10] inorganic,[11] and biomolecule[12,13] materials have been assembled by bottom up methods utilizing electric field,[14,15] magnetic field,[16] flow field,[17] and even functional surface[18] that have advantages over serial approaches such as electron beam lithography,[19] direct laser writing (DLW),[20] and dip-pen lithography.[21] Recently, the responsive 3D microstructures could be manufactured by using virus building blocks[12] and electrodynamic focusing of charged aerosols was also developed for the building of 3D nanoparticle structures.[15,22] An approach using a nano-pipette was successfully demonstrated to realize 3D printing of metals.[23] Methods utilizing DNA structures were recently shown for manufacturing 3D micro/nano structures at atmospheric condition.[13,24] However, it still remains challenging to build versatile three dimensional micro/nanostructures in a practical and scalable way.

In other words, the parallel method for the nanomaterial positioning and assembly that is enabled at atmospheric condition is preferred to be developed for controlling the size and shape in a three dimensional space.

The Ion Assisted Aerosol Lithography (IAAL) that our group developed previously was shown to precisely position through ion induced electrostatic lens and deposit the charged aerosols generated by the spark discharge, arc discharge, electrospray, and evaporation & condensation method[15,22,25] in a parallel fashion. It was also demonstrated that it could produce various three-dimensional structures such as flower structures and floating bridge structures[22] in a parallel way at atmospheric condition. Recently, this method that can produce a simple suspended micro bridge structure consisting of nanoparticles was further developed to manufacture interconnect.[26] However, these previous studies never demonstrated the fabrication of complicated multi-directional grown 3D structures. Furthermore, fundamental mechanism for producing compact 3D microstructures has not been elucidated. Therefore, it still needs further investigation to find a way for fabricating versatile new 3D micro/nanostructures like the multi-furcated 3D structures consisting of nanoparticles and multi-directional 3D interconnecting structures for novel applications.

In the present study, using the assembly of charged aerosols via spatial differentiation of electric field, we present a simple yet practical method to realize multi-directional 3D micro/nanostructures. A combination of generating charged

aerosols by spark discharge and manipulating 3D electric field together with ion-induced electrostatic lenses results in the formation of exotic 3D multi-furcated structures consisting of nanoparticles. To understand the multi-furcation bridging phenomenon, we have done the local electric field calculations and particle accumulation simulations. Based on the simulation, we could demonstrate that the compact nanoparticle assemblies are possible only with the poor conductivity of the resulting structures. Otherwise, the irregular dendritic assemblies could occur as the resulting structures and avoid the air bridges between structures. Using the various arrangement of dielectric pre-patterns on silicone substrate, bi-, tri-, tetra- or penta-furcated 3D nanoparticle structures and even interconnections between neighboring structures are demonstrated.

## **2.2. Methods**

### **2.2.1. Nanoparticle generations and characterizations**

For the generation and deposition of the nanoparticles, the homemade chamber is composed with two chambers which are the spark discharge chamber and electric precipitator chamber. To obtain the high purity nanoparticles, all materials (Cu, Ag, Pd) for the pin and plate in the spark discharge chamber were purchased from Alfa aesar. In addition, high purity nitrogen (99.999 %) helped carrying the untainted NPs from the generating part to the precipitating part. The main gas flow rate was retained constant (2000 sccm) during the spark discharge process by mass flow controller (MFC, MKS), while the flow rate through the corona chamber was 6000 sccm during the pre-process. To generate the stable spark discharge, a high voltage power supply (FUG) was applied (+ 6 kV) to the electric system which was connected with the pin. On the other hand, to collect the positively charged aerosol, - 2kV was applied on the electrode in the electric precipitator chamber. The silicon substrate samples were prepared by the conventional methods like photo lithography and e-beam lithography at KANC (Korea Advanced Nano fabrication Center) (Figure 2.1.). The size distributions of generated nanoparticles were investigated by a scanning mobility particle sizer (SMPS) including aerosol neutralizer (Kr-85), a differential mobility analyzer

(DMA), and condensation nuclei counter (TSI 3022A). By using a transmission electron microscope (TEM), model JEM-2100F (TEM, JEOL), the size and morphology of the particles were measured. Crystallographic information of films composed of particles was analyzed by a D8 advanced X-ray diffractometer (Bruker miller Co.). The morphology of the particle assembly on the silicon substrate was observed by field emission scanning electron microscope imaging (FE-SEM, Sigma, Carl Zeiss) at an acceleration voltage of either 2kV or 10 kV.

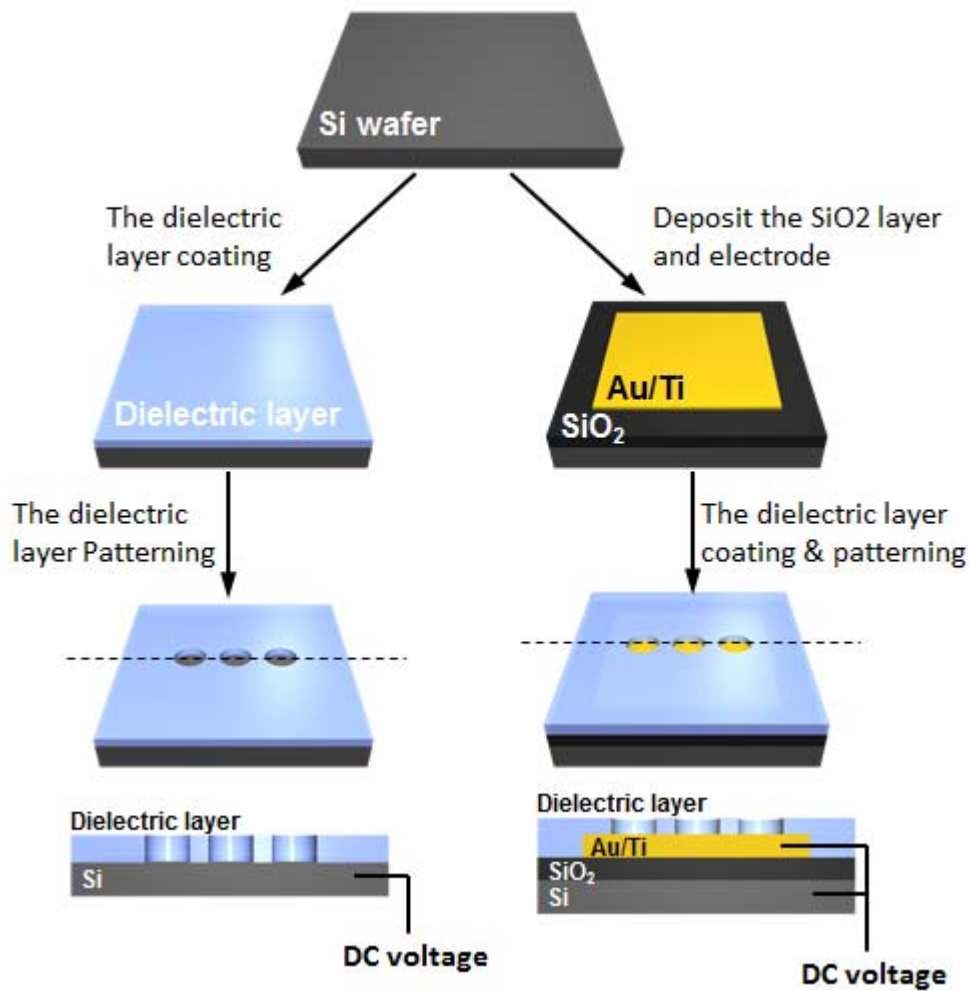


**Figure 2.1.** Preparation of experimental sample with Si wafer. Scheme illustrating fabrication of the silicon substrate and electrode covered with a thin dielectric layer. The dielectric layer has well-shaped patterns with various alignments.

### 2.2.2. Spark discharge and Ion Assisted Aerosol Lithography (IAAL)

Charged aerosol nanoparticles were prepared in gas phase by the pin to plate type spark discharge[27] shown in the upper chamber of our experimental setup (Figure 2.2. (a)) at room temperature and atmospheric pressure. For the proper generation of charged particles, we maintained the operating conditions such as the applied voltage between pin and plate ( $\Delta V_{\text{pin\_plate}} = 6 \text{ kV}$ ), spark frequency ( $f = 30 \text{ Hz}$ ), carrier gas flow rate ( $Q = 2 \text{ slpm}$ ), and material of the pin and plate (all coppers) (Figure 2.2. (a), (b), and (c)). After being generated, small sized nanoparticles (see Figure 2.2. (d) and (e) for size distributions for different metals, see also Figure 2.2. (f) for X-ray diffraction patterns) were promptly transferred into the next chamber along the flow of the carrier gas. On account of the small sized nanoparticles with low Stokes number in the tube at the gas flow rate of 2000 sccm, nanoparticle motions were closely coupled to the fluid motion during this transfer.

In the electrostatic deposition chamber (see the bottom part of Figure 2.2. (a)), nevertheless, motion of nanoparticles could be deviated from gas flow streamlines and follow the electric field since nanoparticles have been electrically charged by the plasma flashing during the spark discharge. Consequently the electric field formed between the grounded chamber wall and the applied electrode could propel and guide the charged aerosols with the Coulomb force (Figure 2.3. ).[28]

Figure 2.4. depicts schematically how charged particles above the substrate are

guided and focused at the particular locus by the developed electric potential acting like a funnel to assemble into bifurcated structure. This virtual electrical mold is affected by the pre-patterned silicon substrate because this substrate has a pre-designated dielectric layer on which positive nitrogen ions generated from the corona chamber during the pre-process or from the spark discharge chamber during the particle generation process are deposited. For example, when a negative potential is applied to the substrate, positive nitrogen ions (shown as red circles) deposit first on the dielectric layer and generate repelling electric field (shown as red arrows) around pre-patterns, which could distort potential field having a funnel shape towards the center opening near the substrate as shown in Figure 2.4. . Therefore, positively charged particles should be guided through these electrical funnels or in other words, electrostatic lens around the pattern. As seen in Figure 2.4. , the final electric field and potential ( $V_{total}$ ) are the outcome of the superposition of electrostatic lenses developed from each individual opening. In this example, we have three openings that generate three electrostatic lenses around each opening. Resulting potential field sketched in Figure 2.4. is the superposition of the above three electrostatic lenses. It means that by changing the arrangement of adjacent hole patterns, three dimensional electric field above the substrate can be manipulated such that charged nanoparticles could be guided to be assembled to become exotic shape of multi-furcated 3D microstructures. As shown in Figure 2.4. for the simplest case of three openings, a bi-furcated

nanoparticle structure is grown from the center hole while asymmetric structures leaning towards to the central structure are grown from each adjacent left and right hole.

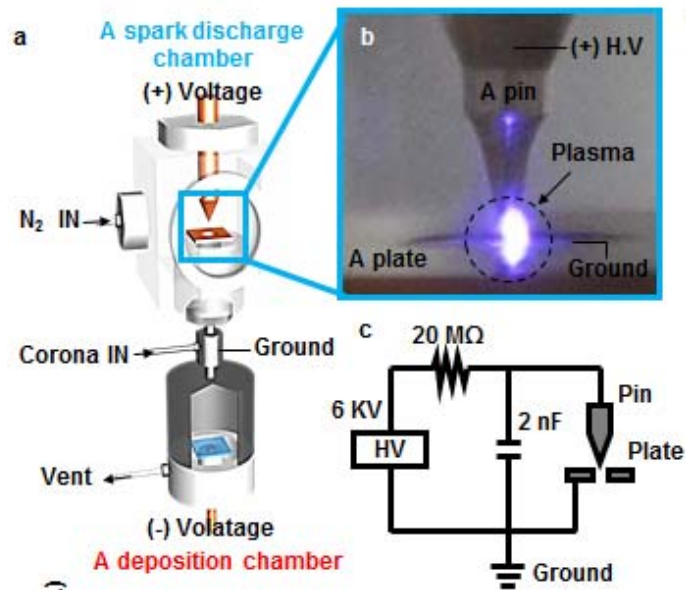


**Figure 2.2.** Experimental setup to generate nanoparticle assembly. a) Schematic of the experimental setup with the systematical connection between a spark discharge chamber and deposition chamber to generate proper nanoparticles. b) Photo of the spark discharge between the pin and plate. c) Schematic of basic electrical system for uniform spark discharge.

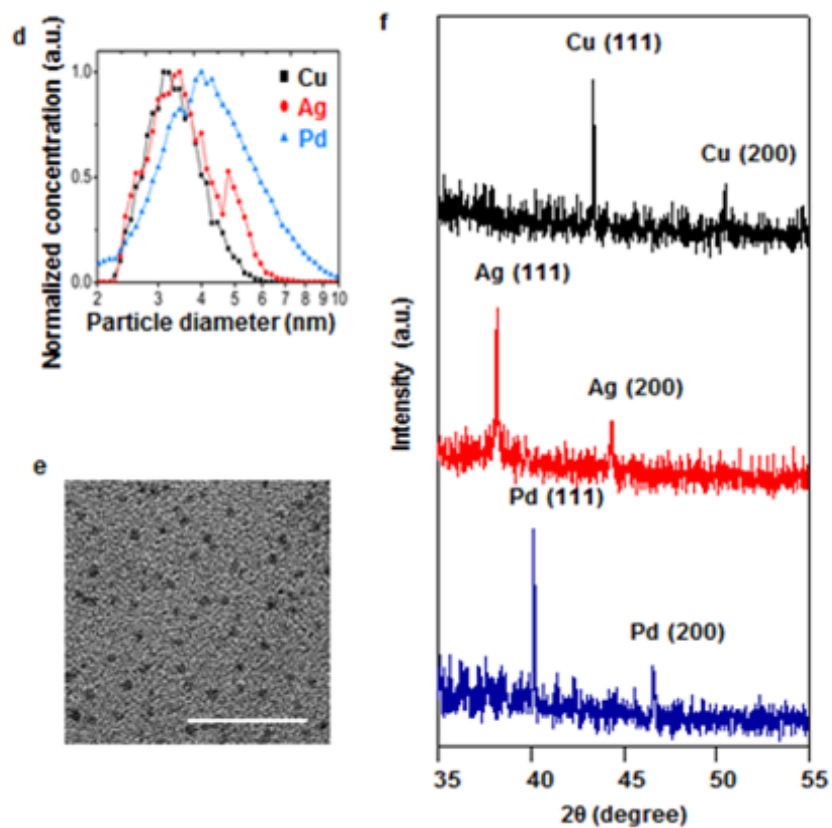


**Figure 2.2.** d) Characterization of the size distribution of Cu, Ag, and Pd nanoparticles with SMPS and (e) TEM image of Cu nanoparticles. Scale bar, 50  $\mu\text{m}$ . (f) is the XRD data of thin films formed with Cu, Ag, Pd nanoparticles.

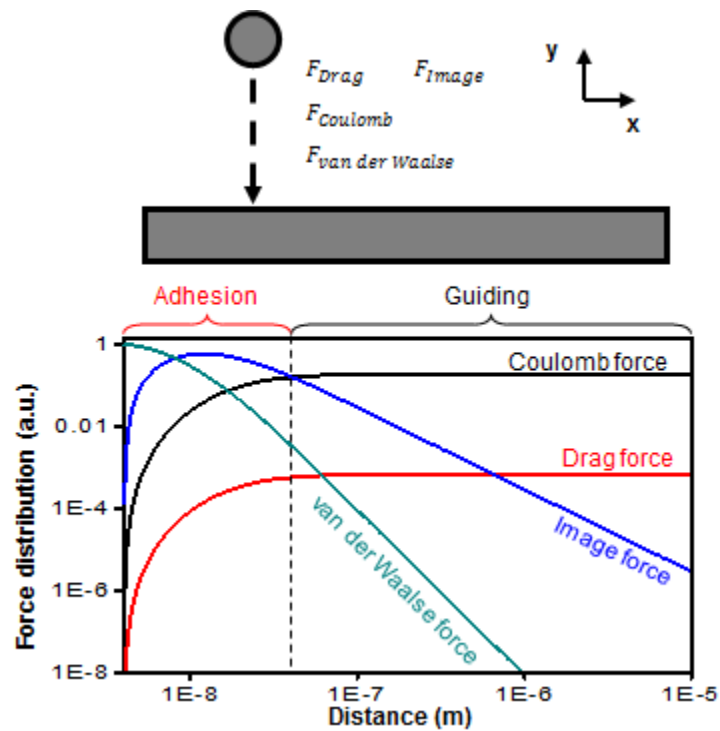


**Figure 2.3.** Comparison of the different forces acting on an incoming particle in the vicinity of the Si substrate. The charged copper nanoparticles ( $d = 4$  nm) are guided by various forces in the experimental setup. Especially some forces like Coulomb force, drag force, image force, and van der Waals force play the important role during the transfer. To calculate the Coulomb force and drag force, the values of electric field and flow velocity at the point of  $100 \mu\text{m}$  from the substrate are used. (Adapted from reference [28].)

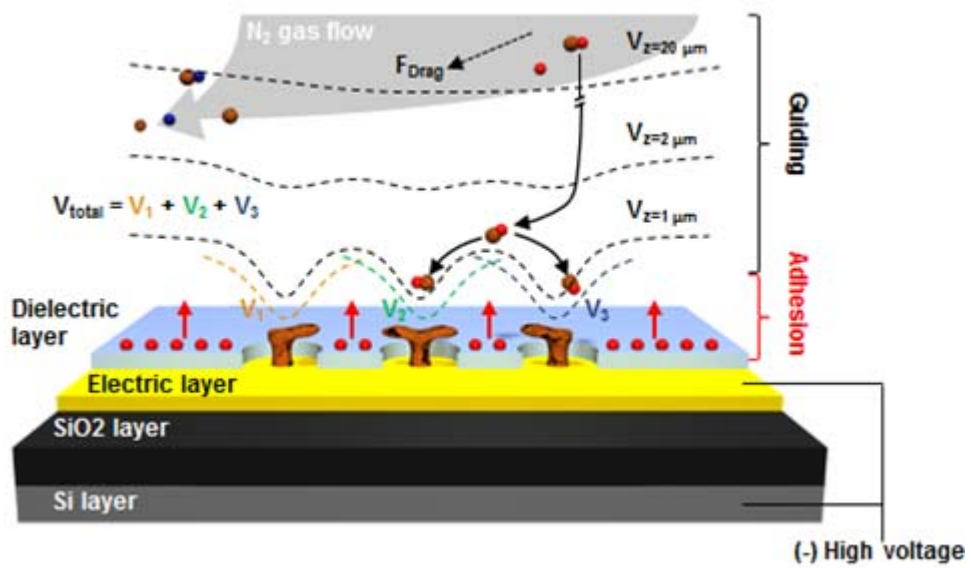


**Figure 2.4.** The electric force directs and guides the charged nanoparticles to the assembly on the substrates. Scheme showing the process to form the nanoparticle (brown balls) assembly by using the electrostatic guiding. The red balls indicate positive charges while the blue balls stand for negative charges. The dashed lines mark the total potentials ( $V_{total} = V_1 + V_2 + V_3$ ) at different heights.

### 2.2.3. Numerical simulation for electric field calculation

To explain how charged particles are assembled, we calculated three dimensional electric fields by solving Maxwell equation (COMSOL 5.1). Simulations of the electric fields above dielectric layer were conducted using COMSOL Multiphysics software in the AC/DC electrostatic module and a particle tracing module with surface charge density  $0.000757 \text{ C/m}^2$  and with relative permittivity of vacuum ( $\epsilon_{\text{gas}} = 1$ ) and of dielectric layer ( $\epsilon_{\text{dielectric}} = 3.2$ ). To obtain the proper electric field near the PR patterns, we calculated the electric field with two steps, the macro and micro domain.[15] In the macro domain calculation (Figure 2.5. (a) and (b)), the electric field in the whole electrostatic precipitator chamber was solved by using the finite element based COMSOL 5.1 program. The calculation region includes the wall of the chamber ( $V = 0 \text{ V}$ ), electrode ( $V = -2 \text{ kV}$ ), and silicon substrate with surface charge. By receiving the data of the macro domain calculation at the boundary surfaces of the micro domain box as the boundary condition, the micro domain calculation was performed like Figure 2.5. (c). To identify the changing electric field according to the growth of the nanoparticle assembly, we conduct the calculation with the five growth steps from  $0$  to  $1.2 \mu\text{m}$  as shown in the red inset. At each growth step, a whole calculation is repeated to obtain the corresponding boundary conditions of the micro domain calculation. Between each of five growth step, we used interpolation for finding proper boundary conditions. As mentioned, nanoparticle

assemblies were assumed to be dielectric.

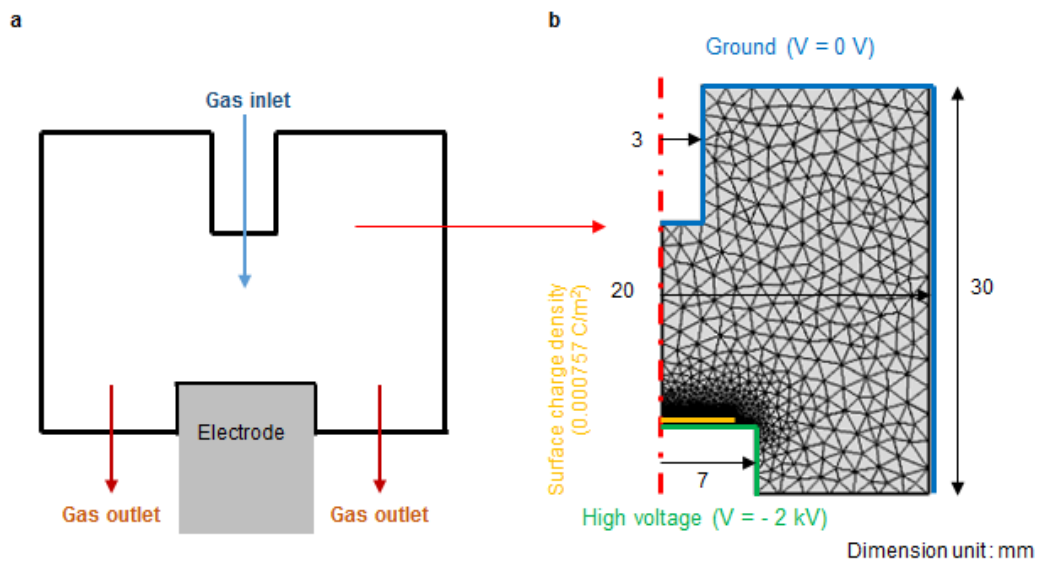


**Figure 2.5.** Procedure to calculate the electric field. a) Crosssectional scheme for the electrostatic precipitator chamber. b) Schematic diagram for the macro domain, which is the interior of electrostatic precipitator chamber.

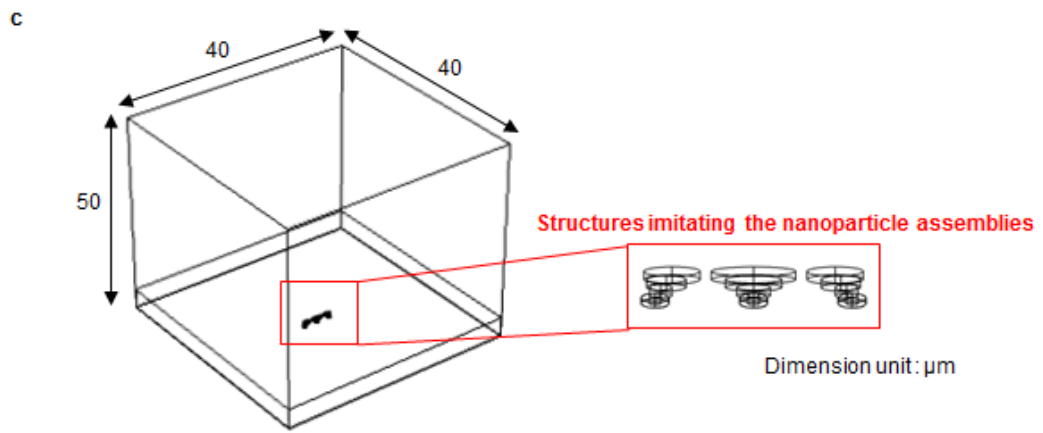


**Figure 2.5.** c) Schematic diagram for the micro domain calculation including the nanoparticle assembly structures.

#### 2.2.4. Homemade Matlab code for the particle trajectory simulation

The particle trajectory and accumulation simulations are performed by the homemade Matlab code[15,22,29] which consider the Coulomb force ( $F_{Coulomb}$ ), drag force ( $F_{Drag}$ ), van der Waals force ( $F_{vdW}$ ), image force ( $F_{Image}$ ), and Brownian diffusion force ( $F_{Brownian}$ ). By solving the 4th-order Runge-Kutta method, the Langevin's equation is calculated for the particle trajectory with the calculation region, 18  $\mu\text{m}$  and 18  $\mu\text{m}$ .

$$F_{Particle} = m_p \frac{d v_p}{dt} = F_{Coulomb} + F_{Drag} + F_{vdW} + F_{Image} + F_{Brownian}, \quad (1)$$

where  $m_p$  is particle mass and  $v_p$  is velocity of particle.  $F_{Coulomb}$  is Coulomb force given by

$$F_{Coulomb} = qE, \quad (2)$$

where  $q$  is charge of particle and  $E$  is electric field around the particle. The electric field is calculated with the surface charge density of the dielectric layer ( $0.000757 \text{ C/m}^2$ ) and boundary potential. Especially the upper boundary condition has the changing potential from -1991.2 to -1991.9, which is solved by COMSOL 5.1 program according to the growth of the structure, while bottom has the fixed voltage, -2 kV.  $F_{Drag}$  is drag force given by

$$F_{Drag} = f (v_g - v_p), \quad (3)$$

where  $f$  is friction coefficient ( $f = 3\pi\mu d_p/C_C$ , where  $\mu$  is the viscosity of the gas,  $d_p$  is the particle diameter, and  $C_C$  is the Cunningham correction factor) and  $v_g$  is flow velocity. [30]  $F_{vdW}$  is van der Waals force acting with a short range

distance from the particle.

$$F_{vdW} = \frac{A_H p g s d_p^3}{12(D_{C,S} - (d_p/2))^2 (D_{C,S} + (d_p/2))^2} \mathbf{n} + \frac{A_H p g p d_p^6}{6(D_{C,S} - d_p)^2 D_{C,C}^3 (D_{C,S} + d_p)^2} \mathbf{r}, \quad (4)$$

where  $A_H$  is the Hamaker constant,  $D_{C,S}$  is the distance between the center of the particle and substrate surface, and  $D_{C,C}$  is the distance between the centers of particles.[31,32]  $F_{Image}$  is the image force acting on the charged particle.

$$F_{Image} = \frac{(qe)^2}{4\pi\epsilon_g(2D_{CS})^2} \cdot \frac{\epsilon_p - \epsilon_s}{\epsilon_p + \epsilon_s} \mathbf{n} + \left( \frac{D_{CC}r_p(qe)^2}{4\pi\epsilon_g(D_{CC}^2 - r_p^2)^2} - \frac{D_{CC}r_p(qe)^2}{4\pi\epsilon_g(D_{CC} + r_p)^4} \right) \mathbf{r}, \quad (5)$$

where  $\epsilon_g$ ,  $\epsilon_p$ , and  $\epsilon_s$  are the relative dielectric constant of the gas, particle, and substrate surface.[33,34] Brownian diffusion force at each time step is given by

$$F_{Brownian} = \sqrt{\frac{2k_B T f}{\Delta t}} \zeta, \quad (6)$$

where  $k_B$  is the Boltzmann constant,  $T$  is the temperature and  $\zeta$  is the zero-mean, unit variance Gaussian random number.[35]

## **2.3. Results and Discussion**

### **2.3.1. Formation of multi-directional assembly with charged nanoparticles**

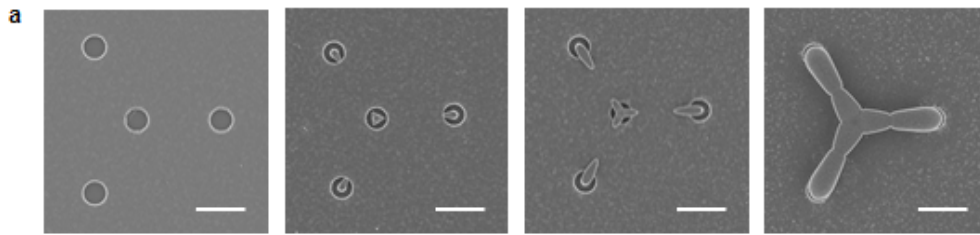
In order to demonstrate the capability of fabricating more complex 3D structures, three hole patterns on the dielectric layer are arranged to encircle the center reference hole with uniform interval (see Figure 2.6. (a)). Initially charged nanoparticles are focused into the center region of each opening through each electrostatic lens developed around each opening and assemble a columnar nanoparticle structure and grow upward. After each structure grows beyond the pattern height, charged aerosol should follow complex electric field that has been formed by superposition of neighboring three electrostatic lens fields (will discuss more later). As can be seen from the second panel of Figure 2.6. (a), due to the superpositioned electric field mentioned above, nanoparticle assembled structures from encircling three holes change their initial vertical growth direction into lateral growth toward the center and the nanoparticle assembled structure grown from the center hole now has three growth directions toward encircling three structures. After some time, the center structure becomes tri-furcated structure similar to three pointed star shape (see the third panel of Figure 2.6. (a)) while three structures around the center structure become more asymmetric structure leaning toward to the center structure. Finally, all four structures are connected to

become multidirectional interconnect that is floating over the substrate like three bridges connecting three holes and center hub (see the fourth panel of Figure 2.6. (a)).

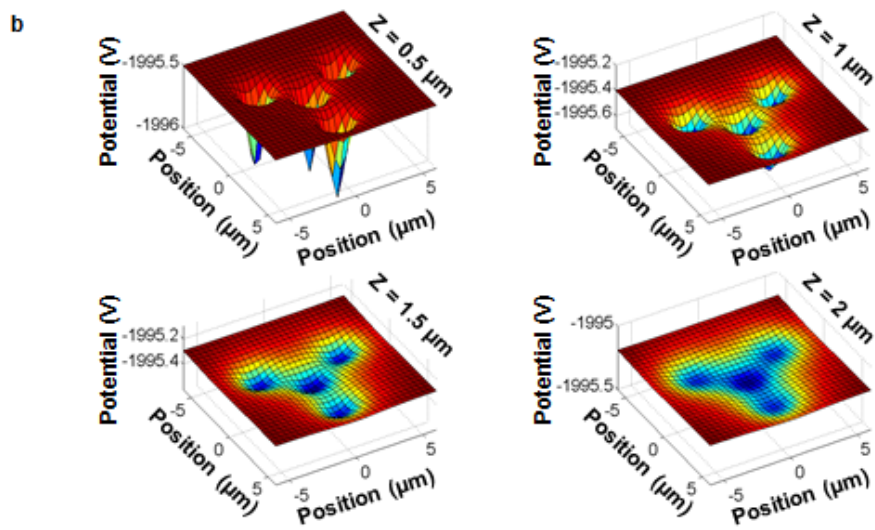
To explain how charged particles are assembled, we calculated three dimensional electric fields by solving Maxwell equation (COMSOL 5.1). Figure 2.6. (b) shows plane views of potential field for four different heights  $Z= 0.5, 1, 1.5$  and  $2 \mu\text{m}$ . At  $Z= 0.5$  and  $1 \mu\text{m}$ , potential fields look like three valleys and saddle and each valley is directed to the centers of three encircling holes and the central hole, which could explain how charged nanoparticles are initially focused into each hole pattern and assembled to grow upward. As the vertical distance becomes farther from the pattern, for example,  $Z= 1.5$  or  $2 \mu\text{m}$ , valleys are all connected (see blue region in Figure 2.6. (b)), which could explain how charged particles are assembled to be connected like the structure shown in Figure 2.6. (a) (fourth panel).

Figure 2.6. (c) shows the particle traps which are influenced by potential peaks electrically separating the regions between the growing structures. It is possible for charged particles with the Brownian motion to cross over the potential peaks and settle down to the region determined by the potential valleys. Simulation of particle motion considering Brownian random force and Coulomb force has been done(will be shown later). Figure 2.6. (c) clearly shows particles are trapped in each valley for a small number of particles, but as particle number is increased,

they are beginning to be connected each other, which could be interpreted to simulate how multidirectional interconnect shown in Figure 2.6. (a) could be assembled. More detailed particle trajectory simulation and examples will be followed below.



**Figure 2.6.** Formation and analysis of tri-directional assembly with charged Cu nanoparticles. a) SEM images of 1  $\mu\text{m}$  hole patterns of the silicon substrate according to the different deposition times (0, 5, 15, and 25 minutes). Scale bar, 2  $\mu\text{m}$ .



**Figure 2.6.** b) Calculated electric potential acting on charged aerosols at the different heights. 3D plots of the electric potential computed at different heights 0.5  $\mu\text{m}$ , 1  $\mu\text{m}$ , 1.5  $\mu\text{m}$ , and 2  $\mu\text{m}$ .

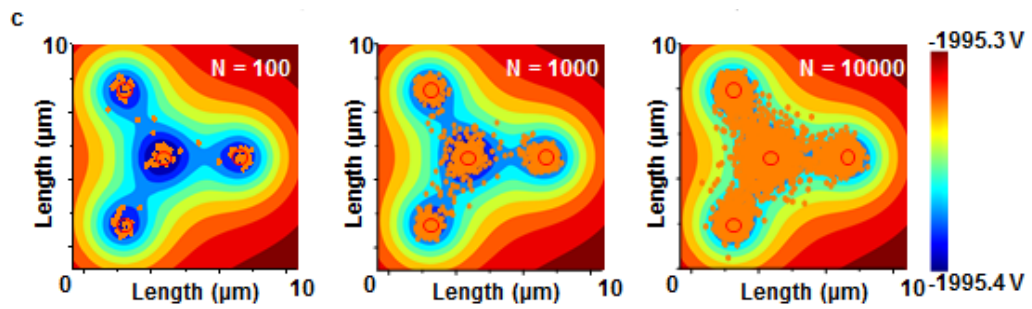


**Figure 2.6.** c) Electrical potential and charged particle (orange colored points, d particle = 4 nm) distributions on the substrate with arranged electrical traps according to the particle numbers ( $N_{\text{particle}} = 100, 1000, \text{ and } 10000$ ) at the height  $Z = 1.5 \mu\text{m}$ .

### 2.3.2. Particle assembly simulation for the bifurcation structure

For simulations of the structure growth with coming charged aerosol nanoparticles we solved the following Langevin equation considering Brownian random force, fluid drag force, Coulomb force, image force and van der Waals force by using our homemade program (details in previous work[22,29]).

$$m_p \frac{dv_p}{dt} = F_{Coulomb} + F_{Drag} + F_{vdW} + F_{Image} + F_{Brownian} \quad (7)$$

As shown in Figure 2.5. (a) and (b), a macro scale calculation was first done, i.e., a whole region of deposition chamber was solved to obtain overall electric field distributions under the given voltage difference and surface charges caused by ion deposition. Then, detailed particle trajectory calculation by solving the above Langevin equation was done only in the microscopic domain shown in Figure 2.5. (c). In this calculation, boundary condition at each boundary of the microscopic domain was obtained from the macroscale calculation aforementioned. Previously[19], these boundary conditions were assumed to be fixed while three dimensional nanoparticle structure was grown and it was also assumed that the growing copper structure was perfectly conductive and thus equipotential while the trajectories of coming particles followed the electric field lines and stuck to the structure. In the present study, we improved these assumptions by considering the time variable boundary conditions that are changing depending on the growth

of 3D nanoparticle structure (details in Figure 2.5. (c)). Also, the assumption of purely conductive structure consisting of about 4 nm copper nanoparticles is now eliminated since the direct resistance measurements (Figure 2.7. ) show that the compact nanoparticle agglomerate should be considered as a very poor conductor due to large inter-grain boundary barriers. Thus, in the present study, the agglomerate is assumed as a dielectric. It is noted that for the previous simulation assuming purely conductive structure, the growth should have been only a Laplace growth (when the particle trajectories are attracted by the sharpest features of the growing structure with the maximum gradient of the potential) which could not simulate actual compact structures nor bridges that were observed experimentally (See Figure 2.8. for morphology of densely packed 3D structure). Furthermore, the previous assumptions of the fixed boundary condition at the micro domain and purely conductive structure erroneously increased electric fields inside the microscopic domain although the focusing of charged aerosols through electrostatic lens and overall assembly process could have been qualitatively predicted.

As Fig. 2.9. shows, the present calculations with improvements mentioned above yield compact structure. Simulations shown in Fig. 2.9. clearly demonstrate that each nanoparticle structure initially grows upward and then the structure grown from the central hole further grows into two split directions (bifurcation assembly) and other structures surrounding the center structure grow leaning

toward the center structure. Also, the previous erroneous increase of electric fields was shown to be eliminated. The resulting agglomerate structure coincides with the shape of the electrical mold/funnel in Figure 2.9. .

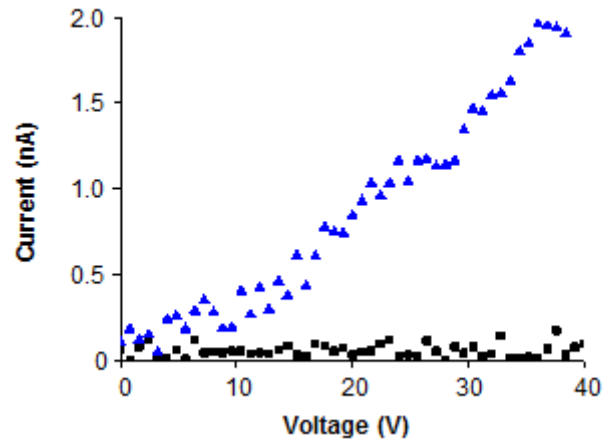


**Figure 2.7.** I-V curve of the Cu nanoparticle assembly. Each of the two datasets corresponds to different states along deposition (■ bare sample, ▲ Cu nanoparticle thin film) over the electrodes with 2  $\mu\text{m}$  gap.

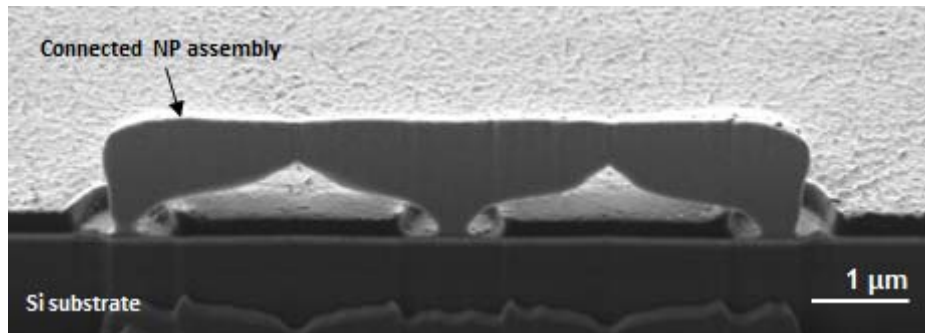


**Figure 2.8.** Cross sectional SEM image of the connected NP assembly by FIB milling.

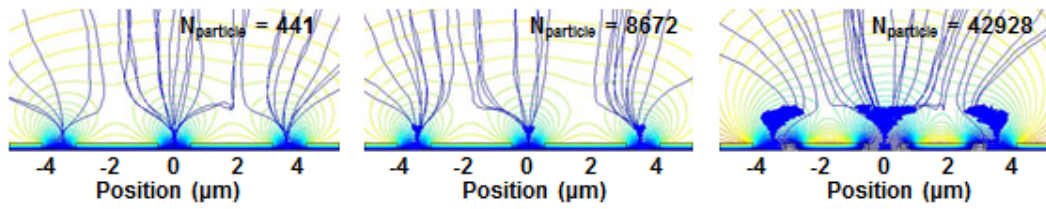


**Figure 2.9.** Two dimensional particle accumulation simulation presents the bridging growth of the particle assemblies while filling the electrostatic virtual mold/funnel thus creating bridges. Particle trajectories are shown in blue.

### 2.3.3. Alignment distance and angle for the bifurcation growth

Consider the simplest line arrangement of holes. Figure 2.10. (a) are the tilted SEM images of the Cu nanoparticle assemblies for three hole patterns arranged in a line with the separation distance of the right hole  $d_1 = 3.5 \mu\text{m}$ ,  $d = 3.5, 7, \text{ and } 14 \mu\text{m}$ , respectively. The potential profile of the electrical mold from COMSOL calculations corresponding to such arrangements of the charged substrate with holes is given in Figure 2.10. (b). Filling up the mold with coming nanoparticles should exactly reproduce the shapes of the assemblies in Figure 2.10. (a).

In order to demonstrate the ability to control the growth directions manipulating with a hole array, we designed hole locations with alignment angles  $\theta = 120, 90,$  and  $60$  degrees shown in Figure 2.11. (a), (b), and (c). One can notice that the structures of  $90$  and  $60$  degrees do not point in the directions of nearby holes. Similar results were obtained in the electric field COMSOL simulations. The calculated data in Figure 2.11. (d) clearly indicate that in the  $60$  degree case the growth direction starts towards the center of the triangle instead of the direction to each hole and bifurcates only later on. It proves that the 3D structure develops by directly filling up the valleys of the potential profile.

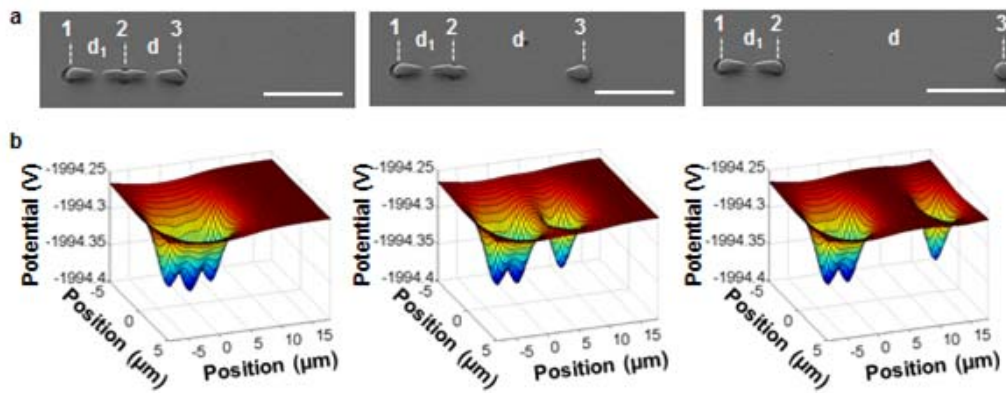


**Figure 2.10.** Manipulation of the growth by well-defined hole location, yielding the bridging assemblies of Cu nanoparticles. a) SEM images for distances  $d_1 = 3.5$   $\mu\text{m}$ ,  $d = 3.5, 7,$  and  $14$   $\mu\text{m}$ . Scale bar,  $5$   $\mu\text{m}$ ; (b) electric potential profile COMSOL calculations for distances  $d = 3.5, 7,$  and  $14$   $\mu\text{m}$  at the height  $Z = 2$   $\mu\text{m}$ .

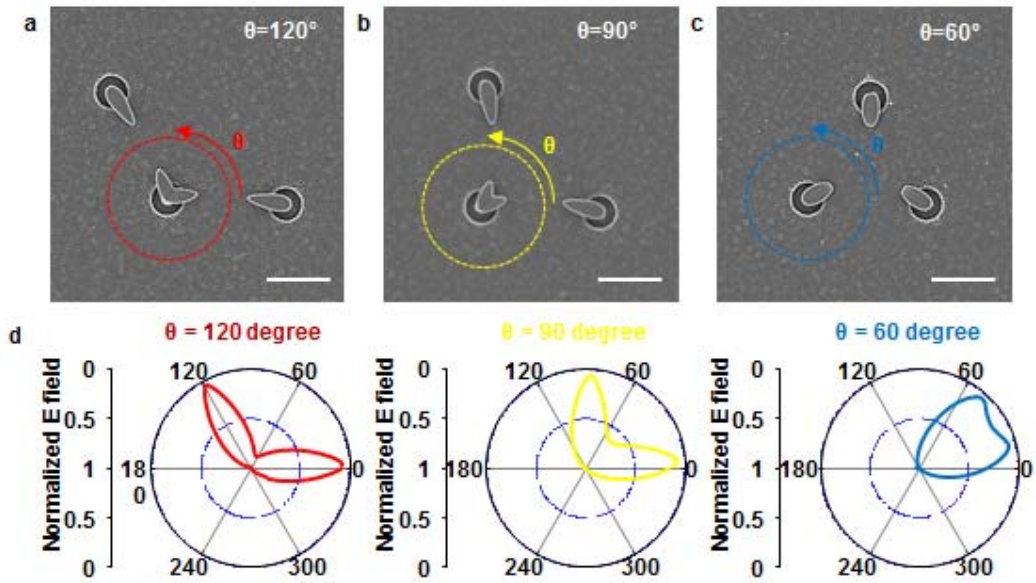
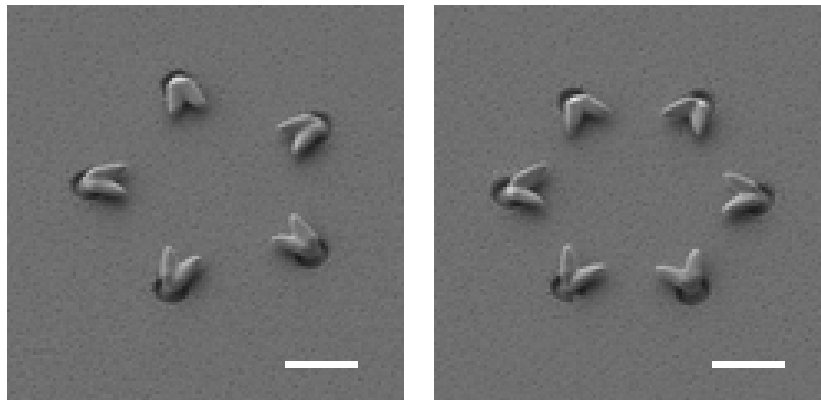


**Figure 2.11.** Programmable Cu nanoparticle assembly for multi-directional 3D structures. a-c) Top view images of nanoparticle assemblies with different arrangement angles ( $\theta = 120, 90,$  and  $60$  degree). Scale bar,  $2 \mu\text{m}$ . d) The calculation results for the normalized electric field ( $E_{normalized} = E/(E)_{Max}$ ,  $E = \sqrt{(E_{tangential})^2 + (E_{radial})^2}$ ) along the dashed lines in (a)-(c) at  $z = 1.5 \mu\text{m}$  that correspond to the shape of the electrical mold to be filled with particles.

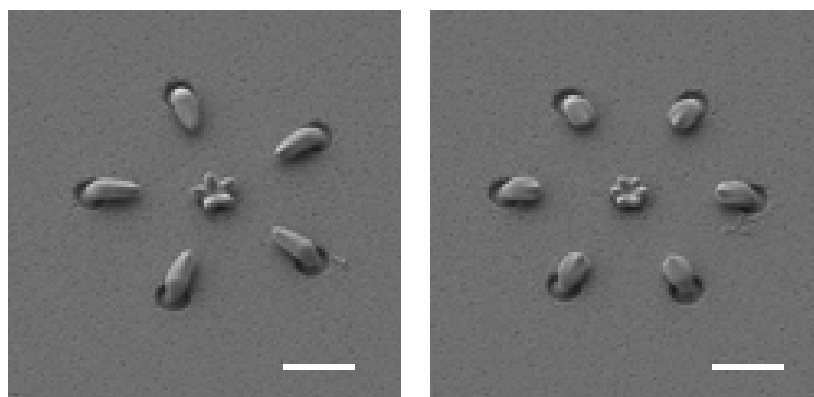
#### **2.3.4. Multi-furcation and spontaneous connections between structures**

Figure 2.12. , 2.13. , and 2.14. present the various nanoparticle assemblies spreading branches along the potential valleys in multi directions. In addition, Figure 2.15. demonstrated that stainless steel nanoparticles could be also assembled in 3D. Thus we could create the penta-, and hexa-furcated structures at the center of the number of surrounded holes with diverse materials.

As the deposition time progressed, the structure eventually met with near structures as the final form (Fig. 2.16. ). This connection between structures along the pre-designed substrate indicates that we can fabricate the multi-directional networks, such as air bridges, with the controlled electric field at the well-defined places. Without the real time precision control and highly accurate design, our approach is still able to generate the air bridges reaching out in multi-directions by the pre-designated hole patterns on the specific areas. For this voluntary connection, the only caveat is to arrange holes around the gap between separated sites. This programmable growth could accordingly be considered as facile strategy to properly connect the separated areas such as electrodes



**Figure 2.12.** Well defined structures are able to be built by the pre-designed hole arrangement. Scale bar, 2  $\mu\text{m}$ .



**Figure 2.13.** Penta- and hexa-furcated assemblies and surrounded asymmetric structures on the substrate. Scale bar, 2  $\mu\text{m}$ .

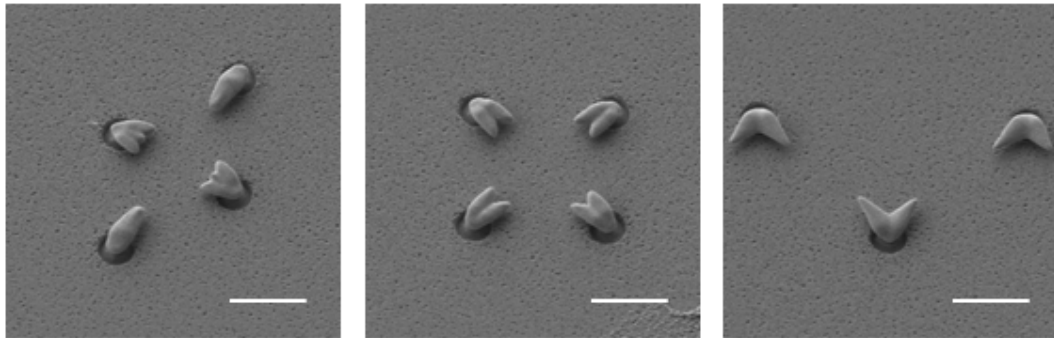


**Figure 2.14.** Various multi-directional 3D assemblies of charged Cu nanoparticles from the well-defined hole pattern array. Well-defined structures are able to be built by well-designed hole pattern arrangement. On the dielectric layer,  $1\ \mu\text{m}$  hole shaped patterns are placed at the same distance ( $d = 3.5\ \mu\text{m}$ ) and various alignment angle. Scale bar,  $4\ \mu\text{m}$ .

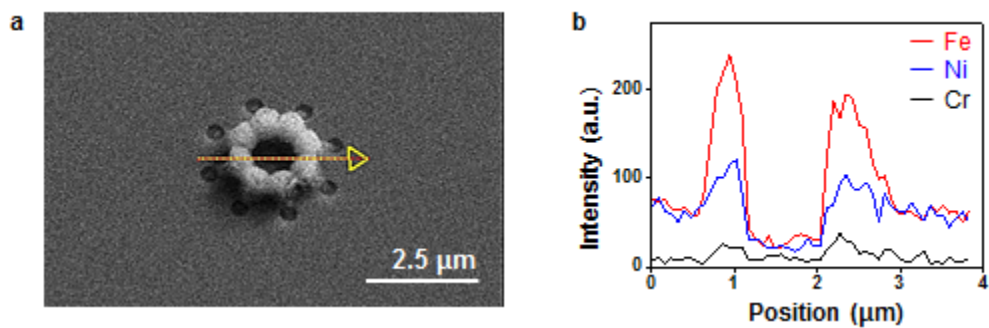


**Figure 2.15.** a) Tilt view SEM image of the stainless steel nanoparticle assembly and (b) linearly element scanning data with EDS along the line on (a).

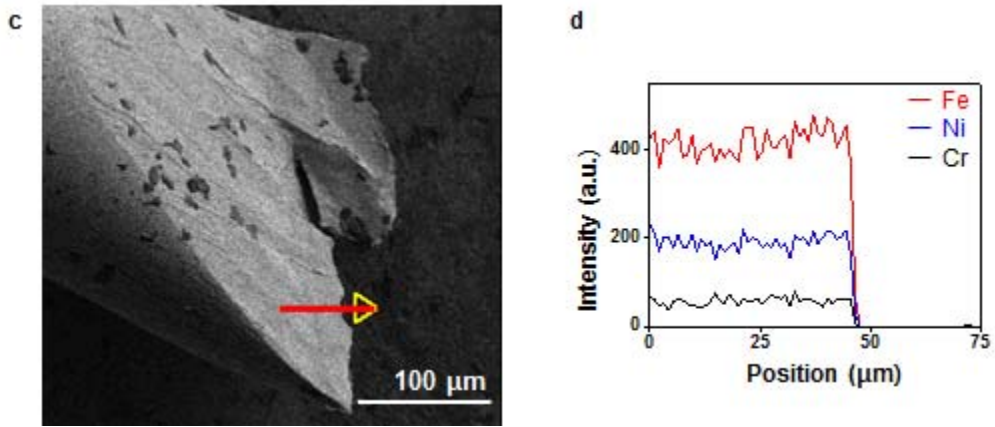


**Figure 2.15.** c) SEM image of the specimen of the stainless steel (SUS-304) and linearly element scanning data with EDS along the line on (c).

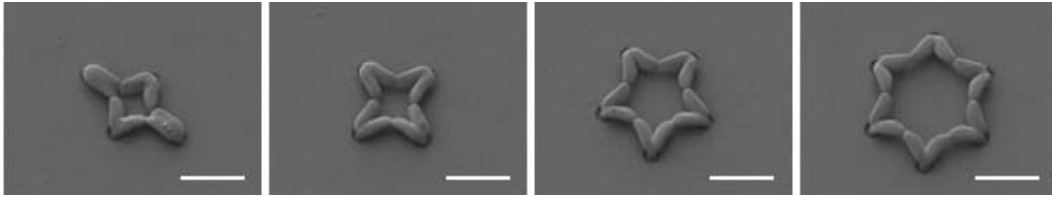


**Figure 2.16.** According to the particle deposition time, the assembly could grow more to the near structure and finally connect between the structures. Scale bar, 4  $\mu\text{m}$ .

## **2.4. Summary**

The present study demonstrates the programmable strategy to assemble charged aerosols in the anisotropic three dimensional structures. We proved that the deposition of charged particles could be controlled by the electrical funnels/molds along the hole patterns on the substrate. The calculations of the electric field and potential above the substrate could be used to design multi-furcated and bridging structures. We expect that this asymmetric assembly of nanoparticles, which stems from the controlled electric field, provides a promising route for developing ordered multi-directional networks and junctions that can be applied to a wide research field such as nanoelectronic circuits, sensors, and other devices.

## 2.5. References

- [1] L. Soleymani, Z. Fang, E. H. Sargent, S. O. Kelley, *Nature Nanotechnol.* 2009, 4, 844.
- [2] A. Tricoli, S. E. Pratsinis, *Nature Nanotechnol.* 2009, 5, 54.
- [3] N. Liu, M. L. Tang, M. Hentschel, H. Giessen, A. P. Alivisatos, *Nature Mater.* 2011, 10, 631.
- [4] R. A. Potyrilo, H. Ghiradella, A. Vertiatchikh, K. Dovidenko, J. R. Cournoyer, E. Olson, *Nature Photon.* 2007, 1, 123.
- [5] W. L. Noorduin, A. Grinthal, L. Mahadevan, J. Aizenberg, *Science* 2013, 340, 832.
- [6] E. Miele, A. Accardo, A. Falqui, M. Marini, A. Giugni, M. Leoncini, F. D. Angelis, R. Krahne, E. D. Fabrizio, *Small* 2015, 11, 134.
- [7] S. Chen, M. Su, C. Zhang, M. Gao, B. Bao, Q. Yang, B. Su, Y. Song, *Adv. Mater.* 2015, 27, 3928.
- [8] K. Ha, E. Jang, S. Jang, J. Lee, M. S. Jang, H. Choi, M. Choi, *Nanotechnol.* 2016, 27, 055403.
- [9] H. Cho, S. M. Kim, Y. S. Kang, J. Kim, S. Jang, M. Kim, H. Park, J. W. Bang, S. Seo, K. Suh, Y. Sung, M. Choi, *Nat. Commun.* DOI 10.1038/ncomms9484.
- [10] P. Akcora, H. Liu, S. K. Kumar, J. Moll, Y. Li, B. C. Benicewicz, L. S. Schadler, D. Acehan, A. Z. Panagiotopoulos, V. Pryamitsyn, V. Ganesan, J. Ilavsky, P. Thiyagarajan, R. H. Colby, J. F. Douglas, *Nat. Mater.* 2009, 8, 354.
- [11] Z. Nie, A. Petukhova, E. Kumacheva, *Nat. Nanotech.* 2010, 5, 15.
- [12] S. Oh, E. Kwak, S. Jeon, S. Ahn, J. Kim, J. Jaworski, *Adv. Mater.* 2014, 26, 5217.

- [13] Y. Ke, L. L. Ong, W. M. Shih, P. Yin, *Science* 2012, 338, 1177.
- [14] A. Rotaru, J. Dugay, R. P. Tan, I. A. Guralskiy, L. Salmon, P. Demont, J. Carrey, G. Molnar, M. Respaud, A. Bousseksou, *Adv. Mater.* 2013, 25, 1745.
- [15] H. Kim, J. Kim, H. Yang, J. Suh, T. Kim, B. Han, S. Kim, D. S. Kim, P. V. Pikhitsa, M. Choi, *Nat. Nanotech.* 2006, 1, 117.
- [16] A. F. Demirors, P. P. Pillai, B. Kowalczyk, B. A. Grzybowski, *Nature* 2013, 503, 99.
- [17] T. Kraus, L. Malaquin, H. Schmid, W. Riess, N. D. Spencer, H. Wolf, *Nature Nanotech.* 2007, 2, 570.
- [18] A. H. Groschel, A. Walther, T. I. Lobling, F. H. Schacher, H. Schmalz, A. H. E. Muller, *Nature* 2013, 503, 247.
- [19] J. D. Fowlkes, R. Winkler, B. B. Lewis, M. G. Stanford, H. Plank, P. D. Rack, *ACS Nano* 2016, DOI: 10.1021/acsnano.6b02108.
- [20] E. Blasco, J. Muller, P. Muller, V. Trouiller, M. Schon, T. Scherer, C. Barner-Kowollik, M. Wegener, *Adv. Mater.* 2016, DOI: 10.1002/adma.201506126.
- [21] J. Zhao, L. A. Swartz, W. Lin, P. S. Schlenoff, J. Frommer, J.B. Schlenoff, G. Liu, *ACS Nano* 2016, DOI: 10.1021/acsnano.6b01145.
- [22] H. Lee, S. You, P. V. Pikhitsa, J. Kim, S. Kwon, C. G. Woo, M. Choi, *Nano Lett.* 2011, 11, 119.
- [23] P. Galliker, J. Schneider, H. Eghlidi, S. Kress, V. Sandoghdar, D. Poulidakos, *Nat. Commun.* 2012, 3, 890.
- [24] B. Ding, H. Wu, W. Xu, Z. Zhao, Y. Liu, H. Yu, H. Yan, *Nano Lett.* 2010, 10, 5065.
- [25] C. G. Woo, H. Shin, C. Jeong, K. Jun, J. Lee, J. Lee, H. Lee, S. You, Y. Son,

- M. Choi, *Small* 2011, 7, 1790.
- [26] J. Fang, L. Schlag, S. Park, T. Stauden, J. Pezoldt, P. Schaaf, H. O. Jacobs, *Adv. Mater.* 2016, 28, 1770.
- [27] K. Han, W. Kim, J. Yu, J. Lee, H. Lee, C.G. Woo, M. Choi, *J. Aerosol Sci.* 2012, 52, 80.
- [28] T. J. Krinke, K. Deppert, M. H. Magnusson, F. Schmidt, H. Fissan, *J. Aerosol Sci.* 2002, 33, 1341.
- [29] S. You, M. Choi, *J. Aerosol Sci.* 2007, 38, 1140
- [30] W. C. Hinds, *Aerosol Technology: Properties, Behavior, and Measurement of Airborne Particles*, Wiley, New York, USA 1999.
- [31] J. Visser, *Interface Sci.* 1972, 3, 331
- [32] J. israelachvili, *Intermolecular and Surface Forces*, Academic Press, London, UK, 1992.
- [33] T. B. Jones, *Electromechanics of Particles*, Cambridge University Press, New York, USA, 1995.
- [34] R. K. Wangsness, *Electromagnetic fields*, Wiley, New York, USA, 1986.
- [35] A. Li, G. Ahmadi, *Aerosol Sci. and Technol.* 1992, 16, 209

## **Chapter 3.**

# **Enhancement of the Metal Oxide Gas Sensor using Nano- aerosol Assembly Structures**

### **3.1. Introduction**

Semiconductor metal oxide (SMO) gas sensors have been widely investigated and industrialized since the first proposal for the SMO gas sensor in 1962 by Seiyama et al. and Taguchi.[1,2] Due to the abundant raw materials, good sensing property, and simple sensing mechanism, many researchers have studied the SMO gas sensor to enhance reaction to the chemical composition of surrounding atmosphere. Recently, to achieve the high sensitivity, nanoscience together with novel fabrication strategies have been investigated. Due to the high surface to bulk ratio, the nanostructured gas sensors are expected to demonstrate increased responses in comparison with the bulk and microcrystalline materials. In principle, the surface reaction between the metal oxide and reaction gas is the basic operating mechanism. So many studies try to enhance the response of the gas sensor, by using thin film gas sensor, controlling the morphology of the nanostructures.[3,4,5]

However, though they present reliability, and fast reaction time, the SMO gas sensors struggle for the sensitivity and selectivity. Especially, for SMO gas sensor, it is not easy to discriminate the mixed gases because of the monotonous reaction of the SMO gas sensors with the specific material. For example, the resistance of the n-type semiconductor metal oxide gas sensors will increase when they meet the various oxidizing gases. On the other hand, when they meet the various

reducing gases, the resistance will decrease. The selective filters allowing the target gases to pass and sensor array composed of sensitive materials have been devised to overcome this nonspecific reaction problem.[6] However, the interfering gases could damage the filters and unpredictable gases could make the noise on the sensing signal through the filter. In addition, despite the enhancement of selectivity, the gas sensor array suffers from some drawbacks like the complex fabrication, high power consumption, large size, and high manufacturing cost.

Recently, instead of thick films, chemical sensors based on the nanostructure are in the focus of attention.[7,8,9] Especially, nanoparticle has emerged as a promising material to improve sensitivity and response time.[10,11] By using spark discharge and aerosol technology, nanoparticles could be continuously generated and properly positioned in the parallel method at room temperature and atmospheric pressure.[12] Also, this ion induced aerosol assembly demonstrated the assembled nanoparticle structures on the substrate, which exhibit the unique optical and electrochemical property as a sensor.[13,14,15]

Here, we report an aerosol based route to generate directly ordered metal nanoparticle assembly and sensitive sensing. Also, we demonstrate the selective sensing of two gases, H<sub>2</sub> and NO<sub>2</sub>, using copper and tin NP assembled bridge structure type sensor. Especially, to discriminate the H<sub>2</sub> and NO<sub>2</sub>, the equations were obtained from the sensing signals and graphical method was employed to estimate the concentration.[6]

## **3.2. Methods**

### **3.2.1. Copper and tin nanoparticle generation and assembly**

The charged aerosol composed of copper and tin nanoparticles were prepared by the spark discharge method at room temperature and atmospheric pressure.[15] While the nitrogen gas was flowing, high voltage was applied between the specific tip and plate to generate spark discharge. By this momentary energy transfer, the material of tip and plate was evaporated in the nitrogen gas and immediately the evaporated material was agglomerated to form the aerosol. For the pure metal nanoparticle generation, the pure metal material was employed in the tip and plate like copper and tin.

After the generation, charged nanoparticles are guided to the electrostatic precipitator chamber by the flow field. However, in the electrostatic precipitator chamber, the electric field also exert the influence to the charged particle's position. Consequently, when negative voltage is applied to the precipitator chamber, positively charged particles and positive ions approach to the substrate. Due to the mobility difference between the ion and charged particle, ions arrive to the surface of the substrate earlier than charged particles and make the electrostatic lens retaining the repulsion force. By using the predesigned opening patterns of the dielectric layer on the substrate, we can control the electric field

near the substrate and structures of the charged nanoparticle assembly. With the two neighboring opening patterns of the dielectric layer, the bridge connecting the electrodes was generated by the nanoparticle assembly.

### **3.2.2. Characterization techniques**

According to the size, the copper and tin aerosols from the each spark discharge chamber were counted by a scanning mobility particle sizer (SMPS) system composed of an aerosol neutralizer (Kr-85), a differential mobility analyzer (DMA, TSI 3085), and a condensation particle counter (CPC, TSI 3776). Also, the morphology of the nanoparticles were analyzed by using a high resolution transmission electron microscope (HR-TEM, JEOL JEM-2100F). The structures of the nanoparticle assembly were observed with scanning electron microscopy (FE-SEM, Sigma, Carl Zeiss) operating at 2 kV or 10 kV.

### **3.2.3. Gas sensor measurements**

For the fabrication of the gas sensor, charged nanoparticles were placed onto the Si/SiO<sub>2</sub> substrate containing Au electrodes separated by a distance of 1  $\mu\text{m}$ . The sample substrates were set in the quartz tube heated by the tube furnace (Figure 3.1. ). The metal nanoparticle assemblies were oxidized for 2 hr at 350  $^{\circ}\text{C}$  under air 500 sccm and stabilized at 300  $^{\circ}\text{C}$  over 12 hr before the gas sensing. The target gas (CO, H<sub>2</sub>, and NO) with dry air as balance gas was flowed into the quartz tube. The various concentrations of the mixture gas were controlled by the mass flow controllers (MFCs) with the constant total gas flow rate (500 sccm). LabVIEW software was used to control remotely and elaborately the gas flow with MFC (MKS). The electrical resistances of the nanoparticle assemblies were measured by digital multi-meter (HP 34401A) connected to a PC.

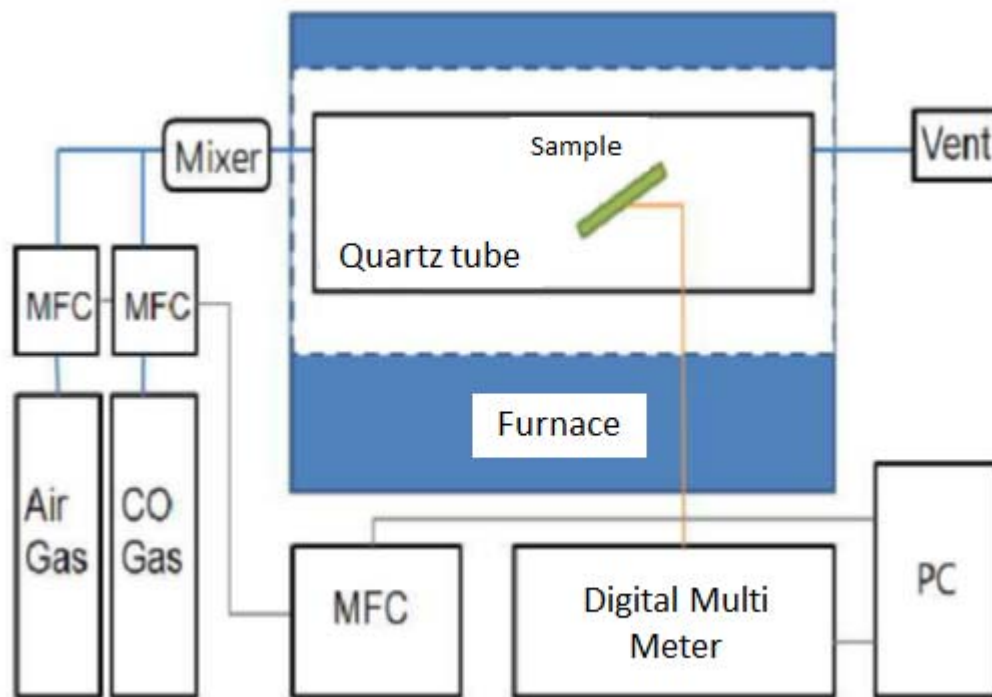


**Figure 3.1.** Schematic of the experimental setup for the gas sensing measurement.

### **3.3. Results and discussion**

#### **3.3.1. Network and interconnection with nanoparticle assembly**

To demonstrate the feasibility of our 3D multi-furcated agglomerate structures for electric devices, the resistance of the Cu nanoparticle assembly was measured in accordance with growth stages as shown in Figure 3.2. (a), (b), and (c). Owing to the gap between the electrodes, the measured resistance was a very large constant during early growth stages while a sweep voltage from 0 to 50 V was applied. On contrast, after the particle deposition for approximately 30 minutes, the connected structures established and then the fully connected structures (Figure 3.2. (b)) could carry a current of 1.2 nA at 50 V. A poor conductor was shown even though the structure has been assembled from copper nanoparticles. Inter-grain boundary barriers caused by contact resistance among particles and also partial oxidation of copper nanoparticles could be attributed to poor conductivity of our 3D agglomerates.

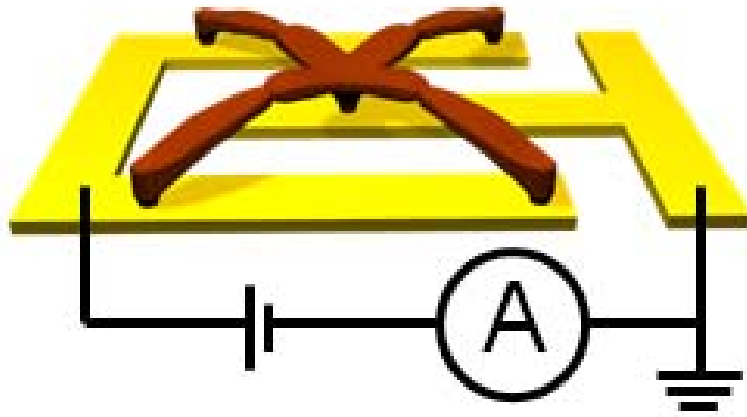


**Figure 3.2.** The electric behavior of the Cu assembly and gas sensing test as an application. a) Scheme illustrating the electrical measurement setup to probe the conductivity of the Cu assembly.

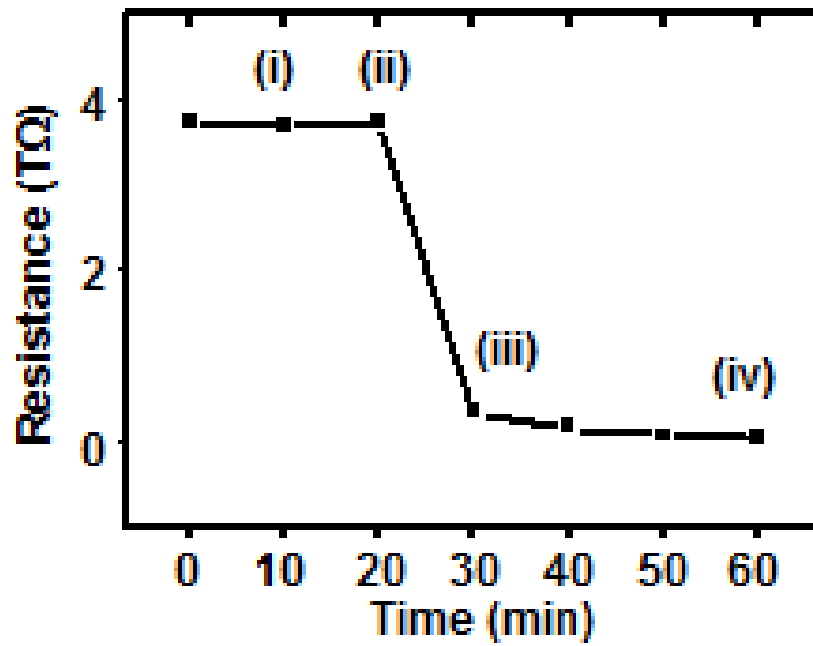


**Figure 3.2. b)** The resistance for the tetra-furcated assembly of Cu nanoparticles according to the growth steps

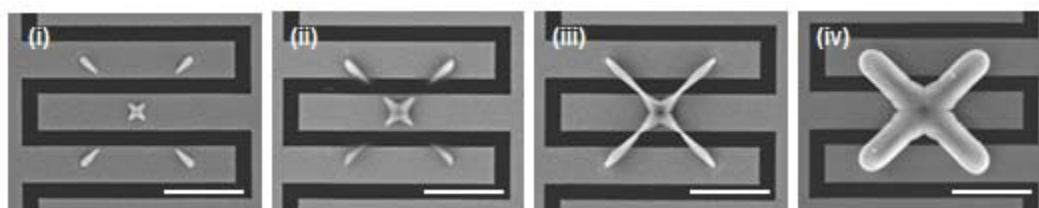
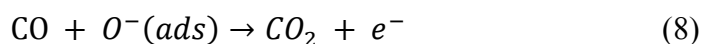


**Figure 3.2.** c) SEM images of tetra-furcated structures developed in time steps.

Scale bar, 4  $\mu\text{m}$ .

### 3.3.2. Sensitivity enhancement with multi-furcation structure of nanoparticle assembly

Copper oxide reacts with reduction gas and also oxidation gas at a proper temperature. At 100-500 °C, oxygen molecules adsorbed onto the surface of copper oxide are ready to respond to CO gas that changes the conductivity of sensing materials as the results of the reaction equation below:



After the oxidation, the copper oxide sensor samples (Figure 3.3. ) were stabilized at the operation temperature 300 °C in air atmosphere and periodically exposed to CO gas mixed with air for 5 minutes (Figure 3.4. , 3.5. , and 3.6. ). In comparison with a nanoparticle thin film type sensor, the tetra-furcated three dimensional structure shows more than a two times higher response to CO at 100 ppm. Moreover, this multi-furcated 3D sensor after being doped with catalyst Pd nanoparticles displays the highest response ( $\Delta R/R_{\text{air}} = 1.75 @ \text{CO } 100 \text{ ppm}$ ). Pd doping was done by using the spark discharge consist of a Pd pin and copper plate electrode. A short-term drift shown in Figure 3.4. , 3.5. , and 3.6. would be attributed to the short time interval which sufficient recovery has not been reached. Figure 3.7. shows that a full recovery can be achieved after sufficient time is given. The same gas sensing performance was confirmed before and after one week maintain at 300 °C (See Figure 3.8. ).

Lower detection limit (LDL) below 1 ppm was estimated for the CuO

nanoparticle bridge structure, which is enough lower than the CO exposure limit.[16] To estimate LDL of the CO gas sensors, first, the calibration function for the sensitivity was fitted and expressed by:

$$S = A \cdot p^B \quad (8)$$

Also, the minimum detectable response,  $S_{min}$ , is defined as

$$S_{min} = S_{Air} + 3\sigma_0, \quad (9)$$

where  $S_{Air}$  is the sensitivity in the air before the gas exposure and  $\sigma_0$  is the standard deviation.[17] Combining the equations and solving for  $p_{min}$

$$S_{min} = A \cdot p_{min}^B = S_{Air} + 3\sigma_0 \quad (10)$$

$$p_{min} = \left(\frac{3\sigma_0}{A}\right)^{1/B} \quad (11)$$

A, B,  $\sigma_0$  and  $P_{min}$  for the gas sensors were obtained and arranged like below figure and table.

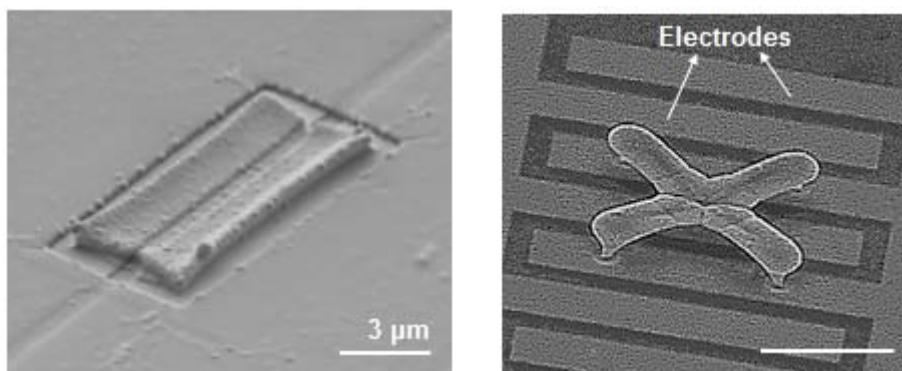


**Figure 3.3.** SEM image of a Cu nanoparticle assembly (film and tetra-furcation bridge structure) for the gas sensor. Scale bar, 5 μm.

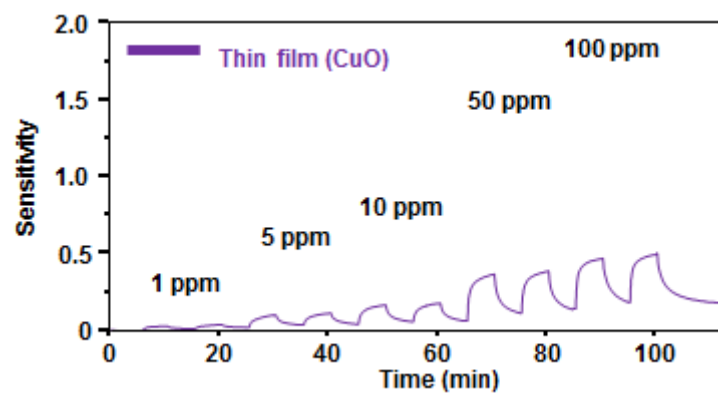


**Figure 3.4.** CO gas detecting behavior for the copper nanoparticle thin film.

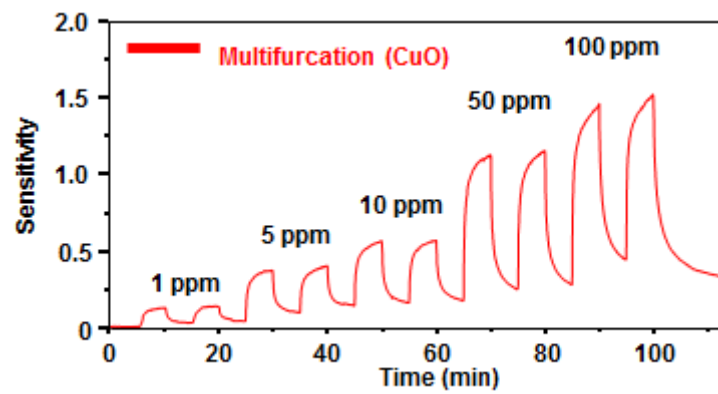


**Figure 3.5.** CO gas detecting behavior for the tetra-furcated structures with only copper particles.

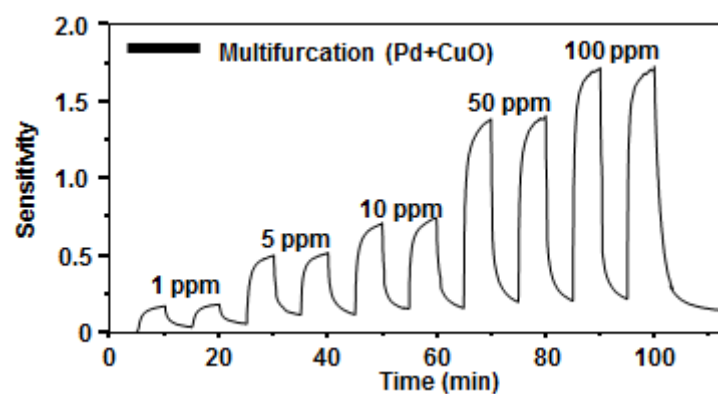


**Figure 3.6.** CO gas detecting behavior for the tetra-furcated structures with palladium and copper nanoparticles.

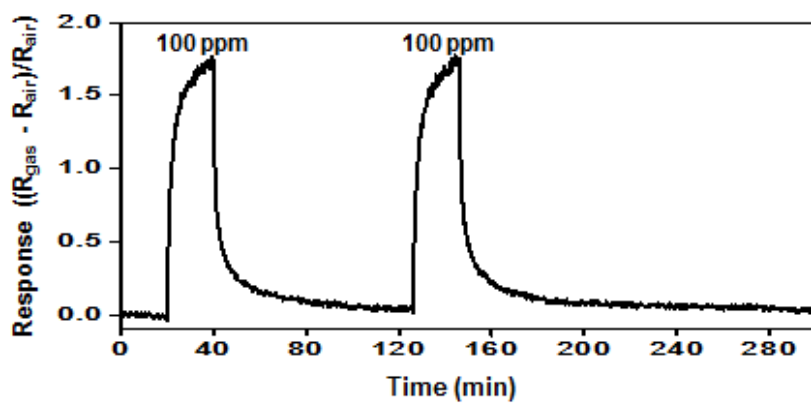


**Figure 3.7.** CO gas detecting behavior of tetra-furcated bridge structure with palladium and copper nanoparticles. The exposed gas concentration is 100 ppm.

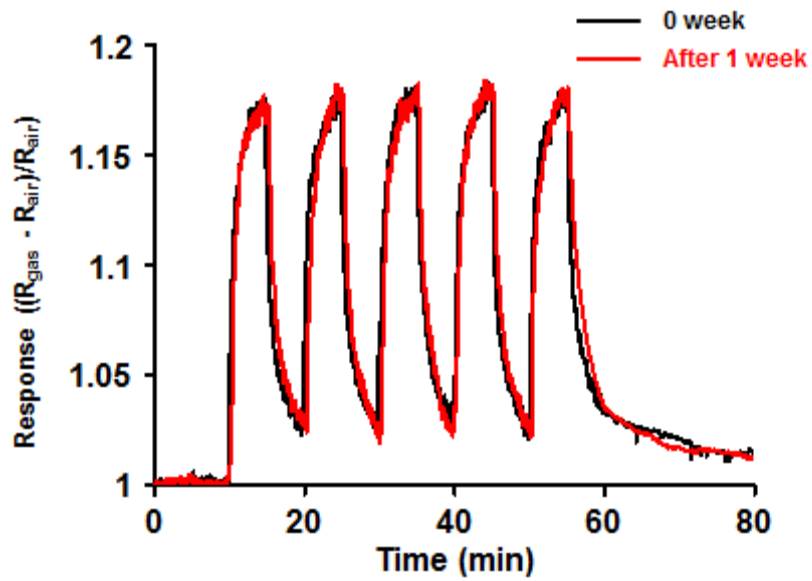


**Figure 3.8.** CO gas detecting behavior of tetra-furcated bridge structure with palladium and copper nanoparticles. The gas sensing experiments were conducted with an interval of one week. During one week, gas sensor sample was on standby at 300 °C. The exposed gas concentration is 10 ppm.

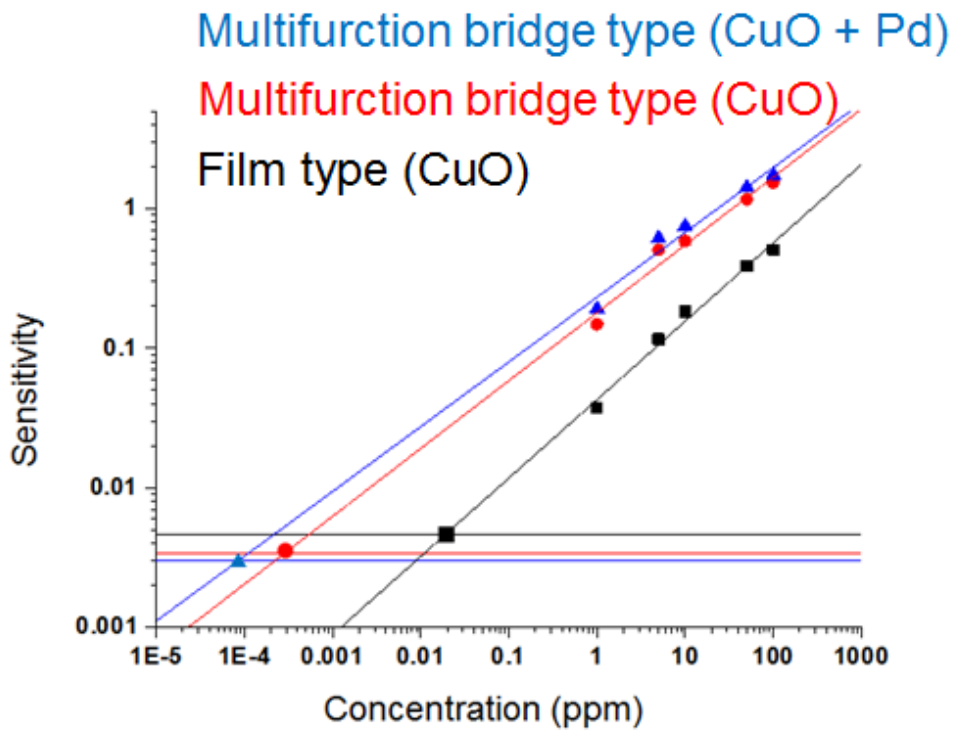


**Figure 3.9.** The extrapolation curves of the sensing response to estimate the low detection limit (LDL) for low CO concentrations.

	A	B	Standard deviation ( $\sigma_0$ )	$P_{\min}$ [ppb]
Film (CuO)	0.0429	0.5616	0.00155	1.9128
Bridge (CuO)	0.1799	0.4862	0.00114	0.0288
Bridge (CuO + Pd)	0.2326	0.46397	0.001	0.0084

**Figure 3.10.** Based on the fitted curves and equation, A, B,  $\sigma_0$ , and  $P_{\min}$  are arranged in the table.

### **3.3.3. Selective detection of NO<sub>2</sub> and H<sub>2</sub> using heterogeneous metal oxide gas sensor array with nanoparticle assembly**

Generally it is difficult to discriminate the gas mixture for the metal oxide gas sensor. Indiscriminate response to the oxidation gas or reduction gas makes challenging to distinguish the gas mixture for the metal oxide gas sensor. In this part, the gas mixture (NO<sub>2</sub> and H<sub>2</sub>) would be estimated by the two kinds of sensing materials (CuO and SnO<sub>2</sub> nanoparticle bridge structure).

Prior to the experiment of the gas sensor with the bridge structure, we needed to check the difference in the sensing performance according to the bridge structures. Based on the operation mechanism of the metal oxide gas sensor, the gas sensing performance could be affected by the contact morphology and cross-sectional area between the near structures.[18, 19] Figure 3. 11. shows the top and tilt view scanning electron microscope images of the Cu nanoparticle assemblies for the bridge structures in accordance with the growth time 15, 20, and 25 minutes. These structures were applied to the gas sensor and exposed to CO 10 ppm for 10 minutes. (Figure 3. 12. (a)) The thinner bridge structure showed the higher initial resistance ( $R_0$ ) and resistance change ( $\Delta R$ ) in response to the sensing. (Figure 3. 12. (b) and (c)) On the other hand, as a result of the definition ( $S = \Delta R / R_0$ ), there was an indistinct difference between the sensitivity of the gas sensors. (Figure 3. 12. (d) and (e))

It is experimentally and theoretically well known that the resistance change of

metal oxide by the single target gas follow the nonlinear power law of its partial pressure. Nevertheless, if the concentration of the target gas mixture is low enough to be ignored, only the reaction between the gas and surface would be considered. In addition, the empirical equation for the multiple gas reaction could be determined with multiplying the each reaction equation. [20]

The equations for the response to the NO<sub>2</sub> and H<sub>2</sub> gas were obtained by fitting the sensing responses of the CuO and SnO<sub>2</sub> nanoparticle bridge structure (Figure 3.13. , 3.14. , 3.15. , and 3.16. ).

$$\begin{aligned} \left(S_{CuO @ NO_2}\right)^{-1} &= 1 + 65238.245 \left(\frac{P_{gas}}{P_{atm}}\right)^{1.2} \\ S_{CuO @ H_2} &= 1 + 148.96591 \left(\frac{P_{gas}}{P_{atm}}\right)^{0.6} \\ S_{SnO_2 @ NO_2} &= 1 + 57826.707 \left(\frac{P_{gas}}{P_{atm}}\right)^{0.8} \\ \left(S_{SnO_2 @ H_2}\right)^{-1} &= 1 + 2276.63 \left(\frac{P_{gas}}{P_{atm}}\right)^{0.5} \end{aligned}$$

These equations were integrated for the each materials to represent the response to the multicomponent gas.

$$\begin{aligned} S_{CuO} &= \left( \frac{1}{1 + 65238.245 \left(\frac{P_{NO_2}}{P_{atm}}\right)^{1.2}} \right) \left( 1 + 148.96591 \left(\frac{P_{H_2}}{P_{atm}}\right)^{0.6} \right) \\ S_{SnO_2} &= \left( 1 + 57826.707 \left(\frac{P_{NO_2}}{P_{atm}}\right)^{0.8} \right) \left( \frac{1}{1 + 2276.63 \left(\frac{P_{H_2}}{P_{atm}}\right)^{0.5}} \right) \end{aligned}$$

Intersection point of these equations could be used to estimate the concentrations of the NO<sub>2</sub> and H<sub>2</sub>. To demonstrate the legitimacy of this method,

we performed the experiment for the two cases. The first gas mixture was NO<sub>2</sub> 50 ppm with H<sub>2</sub> 50 ppm (Figure 3.17. ) and next gas mixture was NO<sub>2</sub> 10 ppm with H<sub>2</sub> 90 ppm (Figure 3.18. ). In the case I, the relative error between the estimated and real concentrations were 8 % and 4.2 % for NO<sub>2</sub> 50 ppm and H<sub>2</sub> 50 ppm gases. In the case II, the relative error between the estimated and real concentrations were 25 % and 2.3 % for NO<sub>2</sub> 10 ppm and H<sub>2</sub> 90 ppm gases. The exceptional error at the low concentration could be induced from the unexpected reaction of the sensing material to low concentration gases and large fitting error at the low concentration gas. It would be improved by using more reliable and stable material at the low concentration gas.

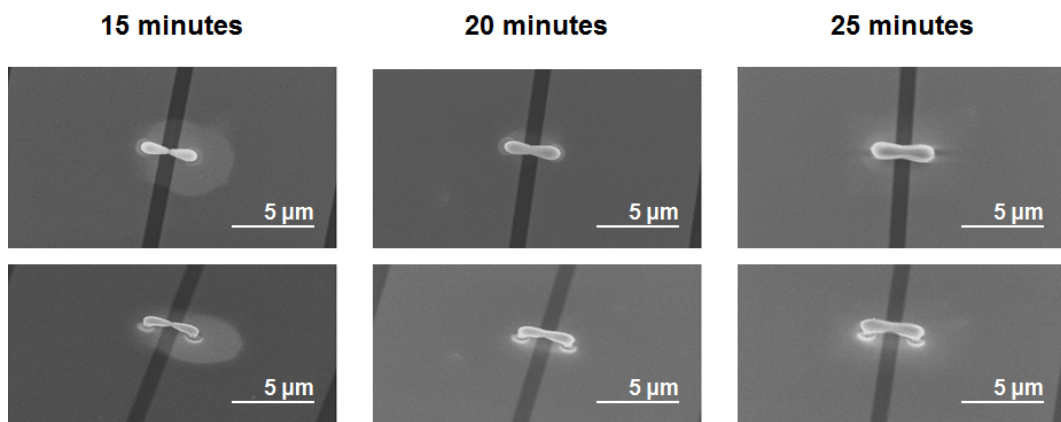


**Figure 3.11.** SEM images of the bridge structures according to the deposition time (15, 20, and 25 minutes).

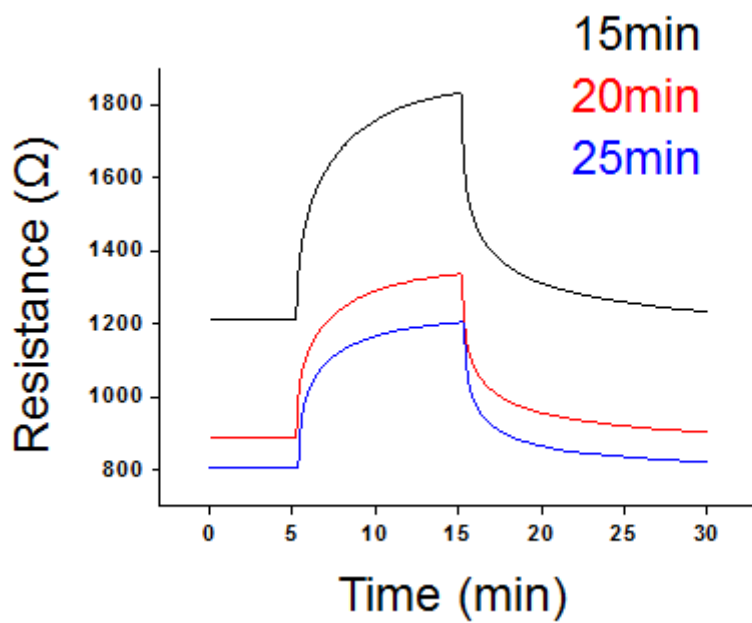


**Figure 3.12.** Sensing response according to the bridge structures. (a) Raw responses of the copper oxide nanoparticle bridge structure to carbon monoxide 10 ppm.

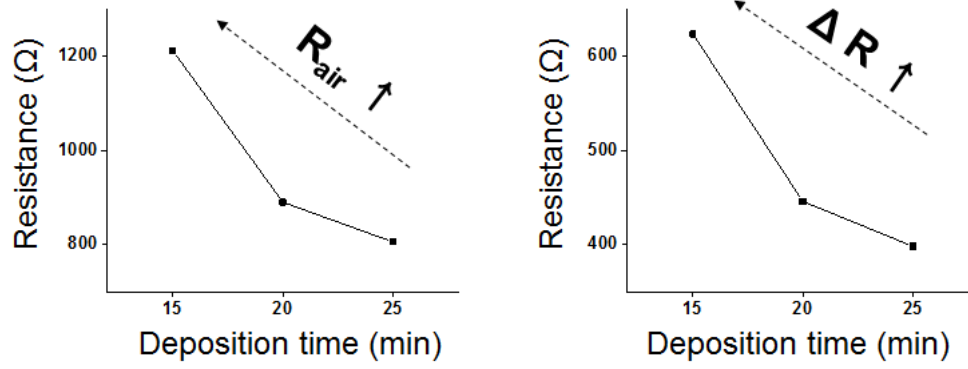


**Figure 3.12.** The comparison of (b) the initial resistance ( $R_{air}$ ) and (c) resistance difference ( $\Delta R = R_{gas} - R_{air}$ ).

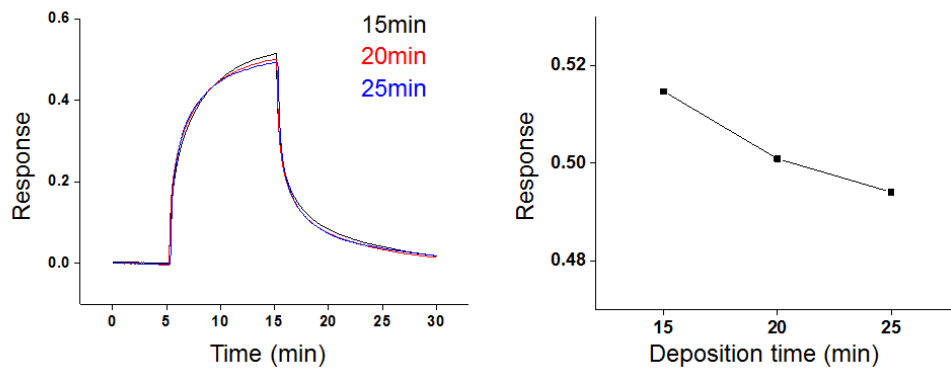


**Figure 3.12.** (d) Sensitivity of the gas sensing response based on the definition ( $S = \Delta R / R_{air}$ ) and (e) the comparison of the sensitivity.

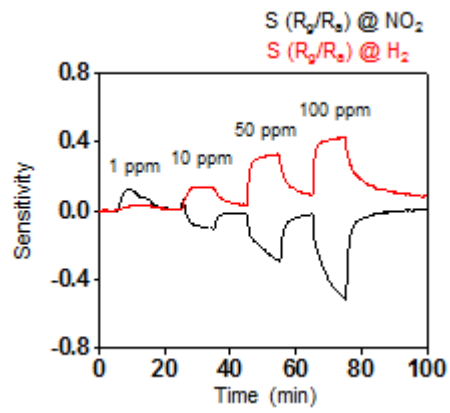


**Figure 3.13.** Gas sensing property of CuO nanoparticle bridge structure to NO<sub>2</sub> (0 – 100 ppm) and H<sub>2</sub> (0 – 100 ppm).

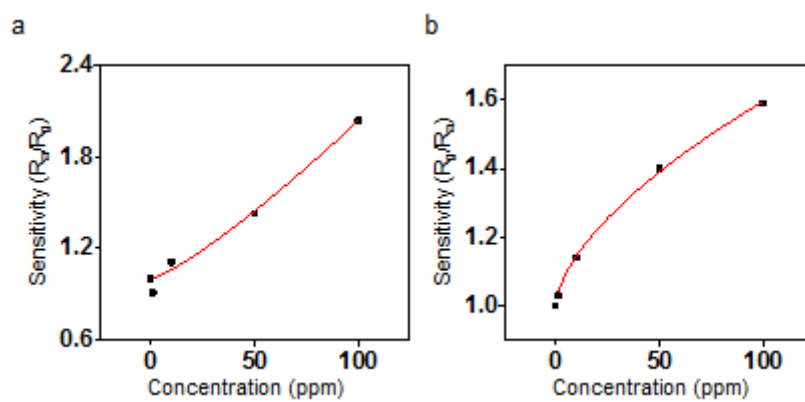


**Figure 3.14.** The fitting line of CuO nanoparticle bridge structure to the a)  $\text{NO}_2$  (0 – 100 ppm) and b)  $\text{H}_2$  (0 – 100 ppm).

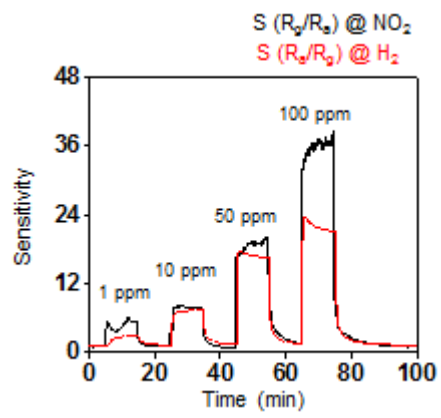


**Figure 3.15.** Gas sensing property of SnO<sub>2</sub> nanoparticle bridge structure to NO<sub>2</sub> (0 – 100 ppm) and H<sub>2</sub> (0 – 100 ppm).

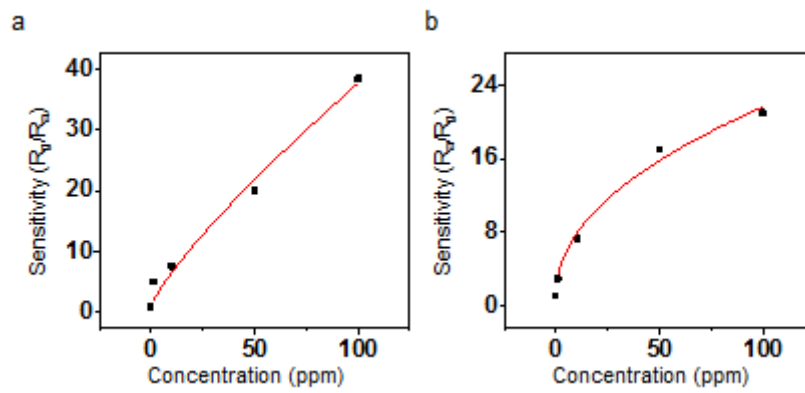


**Figure 3.16.** The fitting line of SnO<sub>2</sub> nanoparticle bridge structure to the a) NO<sub>2</sub> (0 – 100 ppm) and b) H<sub>2</sub> (0 – 100 ppm).

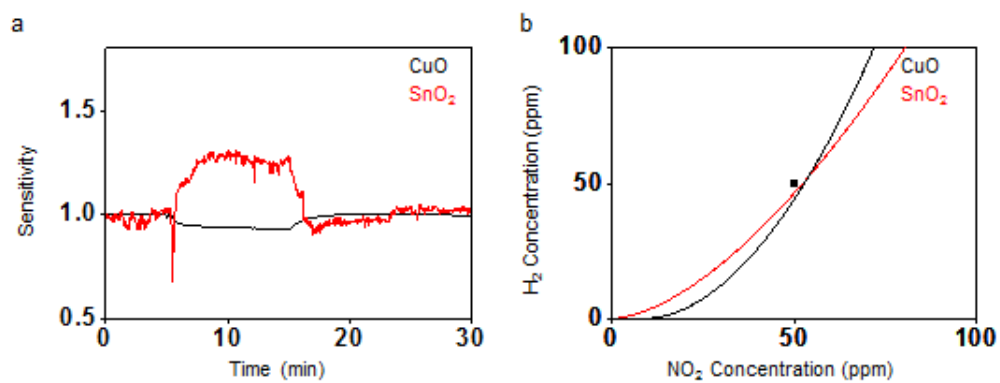


**Figure 3.17.** Sensing response of CuO and SnO<sub>2</sub> nanoparticle assemblies to the gas mixture of NO<sub>2</sub> (50 ppm) and H<sub>2</sub> (50 ppm).

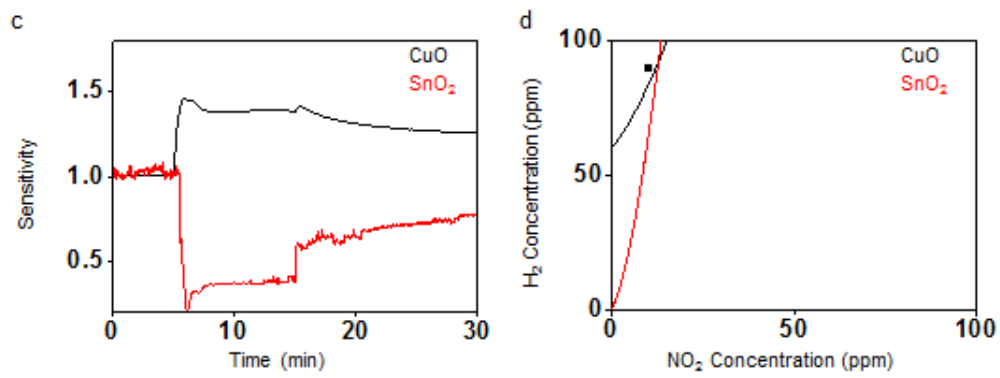


**Figure 3.18.** Sensing response of CuO and SnO<sub>2</sub> nanoparticle assemblies to the gas mixture of NO<sub>2</sub> (10 ppm) and H<sub>2</sub> (90 ppm).

### **3.4. Summary**

First, we have demonstrated the feasibility of the suggested charged aerosol assembly method for electric devices such as a novel gas sensor by fabricating the multi-furcated bridge structures on the Au electrodes. The tetra-furcated bridge structure exhibited excellent gas sensitivity significantly superior to that of two dimensional film type by more than 200 %. And Pd doping could further enhance the sensor response.

Next, we have fabricated the sensor array with the CuO and SnO<sub>2</sub> nanoparticle assembly and conducted the selective detection of NO<sub>2</sub> and H<sub>2</sub>. The mixture gas of NO<sub>2</sub> and H<sub>2</sub> could be estimated with the graphical method for two non-linear equations.

### 3.5. References

- [1] T. Seiyama, A. Kato, K. Fujiishi, M. Nagatani, *Anal. Chem.* 1962, 34, 1502
- [2] N. Taguchi, Patent, 1962, 45-38200.
- [3] A. Tricoli, S. E. Pratsinis, *Nature Nanotechnol.* 2009, 5, 54.
- [4] D. P. Volanti, A. A. Felix, M. O. Orlandi, G. Whitfield, D. J. Yang, E. Longo, H. L. Tuller, J. A. Varela, *Adv. Funct. Mater.* 2013, 23, 1759.
- [5] O. Lupan, V. Postica, V. Cretu, N. Wolff, V. Duppel, L. Kienle, R. Adelung, *Phys. Status Solidi RRL* 2016, 10, 260.
- [6] D. Yang, M. K. Fuadi, K. Kang, D. Kim, Z. Li, I. Park, *ACS Appl. Mater. Interfaces* 2015, 7, 10152.
- [7] L. Soleymani, Z. Fang, E. H. Sargent, S. O. Kelley, *Nature Nanotechnol.* 2009, 4, 844.
- [8] K. Jung, J. Hahn, S. In, Y. Bae, H. Lee, P. V. Pikhitsa, K. Ahn, K. Ha, J. K. Lee, N. Park, M. Choi, *Adv. Mater.* 2014, 26, 5924.
- [9] C. W. Na, H. S. Woo, I. D. Kim, J. H. Lee, *Chem. Comm.* 2011, 47, 5148.
- [10] N. Yamazoe, K. Shimanoe, *Sens. Actuators B* 2009, 138, 100.
- [11] M. E. Franke, T. J. Koplín, U. Simon, *small* 2006, 2, 36.
- [12] H. Kim, J. Kim, H. Yang, J. Suh, T. Kim, B. Han, S. Kim, D. S. Kim, P. V. Pikhitsa, M. Choi, *Nat. Nanotech.* 2006, 1, 117.
- [13] H. Lee, S. You, P. V. Pikhitsa, J. Kim, S. Kwon, C. G. Woo, M. Choi, *Nano Lett.* 2011, 11, 119.
- [14] S. You, K. Han, H. Kim, H. Lee, C. G. Woo, C. Jeong, W. Nam, M. Choi, *small* 2010, 6, 2146.
- [15] Y. Bae, P. V. Pikhitsa, H. Cho, M. Choi, *Adv. Mater.* 2016,

DOI:10.1002/adma.201604159

[16] Health Guidelines for Chemical Hazards (1981- present).

<https://www.cdc.gov/niosh/docs/81-123/>

[17] I. Kim, A. Rothchild, B. H. Lee, D. Y. Kim, S. M. Jo, H. L. Tuller, *Nano Lett.* 2006, 6, 2009

[18] N. Barsan, C. Simion, T. Heine, S. Pokhrel, U. Weimar, *J. Electroceram* 2010, 25, 11

[19] D. P. Volanti, A. A. Felix, M. O. Orlandi, G. Whitfield, D. Yang, E. Longo, H. L. Tuller, J. A. Varela, *Adv. Funct. Mater.* 2012, 23, 1759

[20] D. Yang, M. K. Kang, D. Kim, Z. Li, I. Park, *ACS Appl. Mater. Interfaces* 2015, 7, 10152

## 국문초록

본 논문은 기상에서 전기장의 공간적인 차이를 통해 하전된 에어로졸을 조립하고, 이를 이용해 새로운 다분기 입체 마이크로/나노 구조물을 실현할 수 있는 간단하면서도 현실적인 병행 기술을 다룬다. 스파크 방전에 의한 하전된 에어로졸의 발생 기술과 이온에 의해 유도되는 정전기(electrostatic) 렌즈를 통한 입체적인 전기장 조작 기술이 결합되었다. 이 두 기술의 결합은 나노 입자로 구성된 독특한 3차원 다분기 구조물의 형성으로 이어졌다. 실리콘 기판에 존재하는 비전도층의 프리패턴(prepattern)을 다양하게 배열하고 설계함으로써 2, 3, 4, 또는 5 분기 3차원 나노입자 조립 구조물이 제작되었고, 주변 구조체들 간에 자발적인 연결이 정밀하게 제어되었다. 이 3차원 다분기 마이크로/나노 구조물은 구리 나노 입자로 제작되어 새로운 가스 센서에 응용되었다. 다분기 3차원 구조물을 가진 센서의 경우 필름 형태의 가스센서보다 일산화탄소에 대해서 200 % 향상된 민감도를 보였다. 또한, 이산화 질소와 수소 기체의 선택적 감지를 시연하기 위해 산화 구리 나노 입자와 산화 주석 나노 입자로 구성된 브릿지 (air bridge) 센서 어레이를 제작하고 시험하였다.

**주요어 :** 에어로졸, 나노 기술, 자가 조립, 나노입자 조립, 가스 센서

**학 번 :** 2010-20680